The University *of* Edinburgh

School of Physics
and Astronomy

Directional Dark Matter Detection

MPhys Project Report

Nicolas Angelides

April 26, 2017

Abstract

In this thesis the theoretical capabilities of a 100% polarised, isotopically pure, solid ^{131}Xe detector are tested for signal and background discrimination below the neutrino floor. Through the development and implementation of particle generating algorithms the annual and daily modulation effects were studied for ^{8}B solar neutrino coherent neutral-current angular differential rates and spin independent $6GeV$ WIMP differential rates with nucleon cross-section of $\sigma_0 = 7 \times 10^{-45} cm^2$. The results indicate that polarisation-induced modulation effects are not sufficiently strong to allow for additional discrimination. Annual modulation effects, even though more prominent, would also fail in enhancing discrimination.

Supervisor: Professor A. Murphy

Personal statement

In the first stages of this project I spent most of my time developing the structure and choosing the software libraries that the particle generation and velocity manipulation code would be implementing. Literature review at that early stage was relatively general with a preliminary focus placed on understanding the exact motion described by an observer on the Earth through the galactic Dark Matter (DM) halo. Having reached a point where the code successfully manipulated the required frames of reference and incorporated the relevant velocity contributions a validation stage began. By week four of semester one, the code was confirmed to accurately track the general direction of origin of the DM wind (Cygnus constellation).

I then went on to incorporate the Monte-Carlo algorithms, sampling the initial particle velocity and ensuring that an efficient way to store all the data was in place. By the middle of Semester one I began work on the simplest spin independent differential rate, working through its derivation and finally performing its calculation using the generated particle data. Focus on literature review was now shifting to understanding spin dependent cross-sections and angular dependence. By the end of Semester one, checks on the differential rate of DM WIMP particles had been performed against online sources and the analysis code's proper functionality was confirmed. Focus on literature review was once again adjusted to include the effects of the neutrino background in direct detection.

At the beginning of Semester two, work to incorporate the position of the Sun in the generation code began and its integration had become successful by the start of week three. Having successfully also imported a solar flux model in the Monte-Carlo algorithm, work began on the derivation of the differential rate for the solar neutrino background. At the same time, the spin dependent DM rate calculations were being added to the code and literature review shifted to the status of Xenon freezing and polarisation experiments. Before this time studies were conducted for a spectrum of DM masses while the solar neutrino spectra included both ^{8}B and ^{7}Be. However, I chose to narrow the focus of the study on the first area of the parameter space that the exclusion curves would encounter allowing me to set clearer goals for the end of this project.

Angular differential rates were introduced for both the DM and neutrino signals by the middle of Semester 2 and some initial result interpretation was conducted. Theoretical uncertainties and insufficient background literature in the angular dependence of the DM rates lead me to focus my efforts on the angular dependence of the neutrino's differential rates. After this stage, a lot of time was spent gathering the relevant literature and writing up the background section of this report. Since the the validation of results was a lengthy process, final plots and conclusions were drawn at the very final stage.

Contents

1 Introduction

Approximately eighty-four years have passed since the first observational evidence of the gravitational effects of Dark Matter (DM), yet its identification still remains as one of the most important outstanding questions in particle physics. With a theoretical explanation instantiated by Fritz Zwicky and a later renaissance lead by Vera Rubin, the hunt for DM is now in the focus of several areas within physics. Experimental and theoretical particle physicists, and cosmologists have erected bridges across disciplines in an attempt to accommodate DM and its integration as an extension to the Standard Model of Particles and Interactions. In the endeavour to detect particle DM in the 1-1000GeV/c^2 scale, direct detection experiments have demonstrated leading contributions.

Direct detection of particle DM has first been hypothesised in 1985 [1, 2] and aims to count and measure energy deposits caused by DM-Nucleus scattering events. The detection or absence of energy deposits allows for the exploration of parameter space characterised by a candidate particle's mass and interaction cross-section. Improved instrumentation, larger targets, and longer data taking runs have allowed for the sensitivity to reach lower interaction cross-sections. However this improvement will soon be stopped when a physical process involving neutrinos is expected to dominate and interfere with the discrimination capabilities of future direct detection experiments [3]. Often referred to as the *neutrino floor*, this area of the DM parameter space would become inaccessible to most direct detection experiments due to the indistinguishability of energy deposits caused by neutrino-nucleus coherent scattering and DM-nucleus scattering.

As this is a tremendous obstacle in direct detection, to allow for a future of successfully resolving the parameter space occupied by the neutrino floor, new detector features allowing for the discrimination between neutrino and DM energy depositions have to be implemented [4] while preserving the reach in cross-section. One of the the most prevalent differences of the the DM signal and neutrino background is the direction from which they are expected to originate, allowing detectors with directional sensitivity to *"break through"* the neutrino floor. Target nuclei with net polarisation as well as crystalline planes have demonstrated directional direct detection capabilities and could one day dominate direct detection searches [5, 6].

The following few sections will outline the components required in determining the directional properties of a *polarised frozen Xenon* detector. The importance of and the need for DM will be outlined along side basic principles of direct detection in Section 2. The components incorporated in the software containing the directional information are outlined in Section 3. In Section 4 the results of the implementation of this framework are presented and final conclusions are drawn in Section 5.

2 Background

2.1 Indirect Evidence for Dark Matter

The first instance of discrepancies between observed and predicted trajectories of gravitationally interacting celestial bodies arose as early as the 1930s [7]. The origin of such discrepancies was directly promoted to a question of great importance as it indicated either lack in the understanding of gravity in larger scales or the presence of an unaccounted for type of invisible

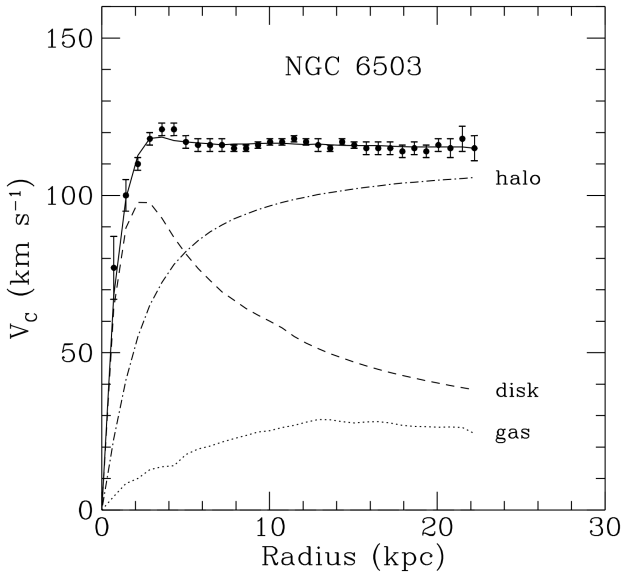

Figure 2.1. Data plotted for the rotation velocities of galaxy NGC 6503 against radial distance from its centre. The dotted, and dashed lines represent contributions from baryonic matter in the gas and galactic disk respectively whereas the dashed-dotted represents the contribution of the DM halo. Data shown to be following the combined effect of the three contributions. Plot taken from Reference [13]

matter called DM. The former of the two paths was perused through theories of Modified Newtonian Dynamics (MOND) that introduce a scale above which gravitational forces deviate from their known form [8]. As now evidence of DM is available across several scales; galaxies, galaxy clusters and cluster filaments, MOND theories have been heavily discredited.

Most famously, the first indirect observation of the need for DM came in 1933 with Fritz Zwicky [9]. Using the measured velocity dispersion of eight individual galaxies in the Coma cluster, Zwicky estimated that the density of the cluster is 400 times higher than what luminous matter indicates.* Even though this number was overestimated due to the use of an incorrect Hubble parameter this observation motivated additional studies of mass-light ratios which yielded similar results in 1936 and the Virgo cluster [10].

In 1939 studies on the rapid revolution of the outer regions of the Andromeda galaxy (M31) by Horace Babcock yielded the first indication of the effects of DM in the galactic scale [11]. While extending the study of galaxy rotations to larger radii in 1976, Vera Rubin and Kent Ford measured the rotation curve for Andromeda and approximated the distribution of DM in the galactic disk [12]. Through this research the first instance of a galactic DM halo was introduced to account for the higher than expected velocities of the outer regions of Andromeda. An example of the rotation curve data plotted against gravitational contributions from the galactic disc and DM halo can be found in Figure 2.1.

Rotation curves of a large number of spheroidal, elliptical and spiral galaxies were since

*The velocity of galaxies was measured using the Doppler width of emitted spectral lines and the cluster mass was estimated using the Virial theorem and measured dispersion velocities

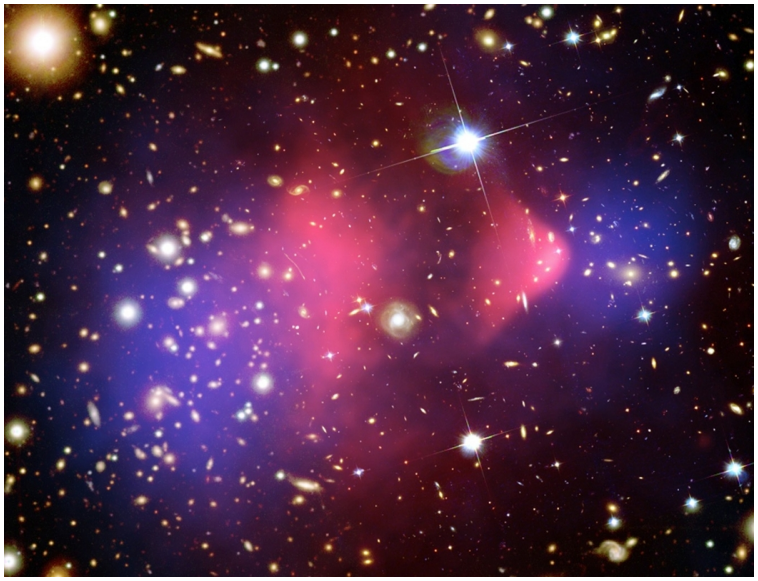

Figure 2.2. Known as *"The Bullet Cluster"*, the structure shown was produced after the collision of two large clusters of galaxies. The areas shaded in pink represent the location of X-Ray emitting gas in the centre of the galaxies of the two clusters. Inferred through gravitational lensing effects, the areas shaded in blue represent regions of high mass density. The lack of distortion in the mass distribution indicates that the majority of mass in the clusters is composed of non luminous collision-less particles. This picture has served as some of the strongest observational evidence for the non-interacting nature of DM. Picture taken from Reference [17]

.

studied [14] and a general agreement has been reached on the distribution of DM in the outermost regions of halos. Uncertainty is still associated with the nature of DM distribution in the region closer to the centres of galaxies [15]. With the rise of large N-body computer simulations, Navarro, Frenk and White have successfully reproduced observed rotation curves implementing the collision-less Cold DM* model [16].

Gravitational lensing had been mentioned in 1937 as a tool form mapping the distribution of DM in clusters. Since imaging satellites have since allowed the more accurate study of these effects, a very important structure has come to the attention of cosmologists. Shown in Figure 2.2, this structure displays the aftermath of a collision (merger) of two galaxy clusters. The distribution of ordinary (luminous) matter shows an expected degree of spread (spallation) due to the strong interactions, however, the lensing effects show a general indifference to the occurrence. This observation does not only confirm the fact that the majority of the matter in the universe is dark but also shows how DM is effectively collision-less.

Additional confirmation for the strong effects of DM also came with the discovery of Large Scale Structure (LSS) in the form of galaxy cluster walls and filamentation, agreeing closely with structure formation simulations [18, 19].

*The distinction between Cold and Warm DM will be made in Section 2.3.1

2.2 Standard Model of Cosmology

In the centre of Theoretical Cosmology a highly accurate model, known as ΛCDM, represents the most precise description of the origin, structure and evolution of the Universe developed thus far. Composed of 6 independent parameters, it accounts for, amongst other key observations, the existence and structure of the Cosmic Microwave Background (CMB), the LSS in the distribution of Galaxies, and the accelerating expansion of the Universe. A key feature of the model is the requirement for the existence and strong contributions of Vacuum (Dark) Energy and Cold DM (CDM) both in the early and later epochs of the Universe. The characterisation of DM as cold refers to its non-relativistic velocities well before a matter-dominated era.

On a cosmological scale, the amount of DM present in the Universe can be derived from the independent parameters in ΛCDM. In the past, this has been conducted through surveys of temperature and polarisation fluctuations in the CMB using the *Wilkinson Microwave Anisotropy Probe* (WMAP) [20]. However, the most recent results on cosmological parameters from the Planck Collaboration combine CMB fluctuations with lensing effects and external data [21]. Planck's most recent publication includes the following derived parameters.

$$\begin{aligned} \text{Dark Energy density parameter} \quad & \Omega_\Lambda = 0.6911 \pm 0.0062 \\ \text{DM density parameter}^* \quad & \Omega_\chi = 0.2589 \pm 0.0057 \\ \text{Baryon density parameter}^\dagger \quad & \Omega_b = 0.0486 \pm 0.0010 \end{aligned} \tag{2.1}$$

As indicated in Equation 2.1, 4.9% of the mass-energy content of the Universe is composed of what is considered as ordinary matter; quarks and leptons. DM, constituting 26%, has been separated as an *unknown* type of matter distinguished by its abundant gravitational interactions (as mentioned in Section 2.1) and named after its non-luminous nature; neither emitting or absorbing any frequency of electromagnetic radiation. The remaining 69% is identified as vacuum, *Dark* Energy, hypothesized to permeate all of space and to be responsible for the observed accelerated expansion of the Universe. ‡

2.3 Particle Dark Matter

Even though evidence for the effects of DM span over several scales, the nature of its constituent is yet to be determined. It should be noted that attempts to account for DM using Baryonic dark objects like Massive Compact Halo Objects (MACHOs) or diffuse Baryons have been presented [22]. Even though the former could account for a small fraction of DM, in the form of large gas giants (Jupiter) or brown dwarf stars, the latter can be excluded from primordial nucleosynthesis constraints.

Particle Theorists recognised the need for physics beyond the Standard Model and a plethora of theories on particle DM has since emerged. Several constraints on the properties of a new particle candidate already exist and should be met by new models [23]. DM particles

*Calculated using $\Omega_\chi h^2$ and $h = H_0/(100 kms^{-1} M pc^{-1})$ where H_0 is the Hubble constant.

†Same as $*$ but with the use of $\Omega_b h^2$.

‡The mass-energy density also includes 0.01% in radiation from the cosmic microwave background and less than 0.5% in relic neutrinos.

would have to be neutral and extremely weakly interacting, as demonstrated in the Bullet Cluster example in Figure 2.2. However, in the thermal history of the Universe, it is expected that DM was in thermal equilibrium with Standard Model particles above a certain "freeze-out" temperature. This temperature fixes the relic density of DM in the Universe and strongly depends on the interaction cross-section (σ) and the particle's relative velocity (v) . An order of magnitude approximation of the DM relic density as shown in Equation 2.2 puts its dependencies in context. Extracted from Reference [24],

$$\Omega_\chi h^2 \approx \frac{3x10^{27} c m^3 s^{-1}}{\langle \sigma v \rangle}. \tag{2.2}$$

To maintain the relic density, particles would also have to be stable with respect to the lifetime of the Universe. Lastly, the candidate has to be compatible with current direct, indirect, and collider search constraints as well as not interfere with models on Big Bang Nucleosynthesis and Stellar Evolution [25]. The parameter space most convenient to represent these models for the purpose of direct detection is the space defined by a candidates' mass against its interaction cross-section with baryonic matter, as shown in Figure 2.3.

2.3.1 Dark Matter Halo

It is important that a DM particle is cold (non relativistic) to allow for the formation of large scale structures and galaxies and ensure their stability. In the simplest of models, a DM particle inside the galactic halo is expected to remain bound, this limits the velocity distribution. In the case of the Milky Way galaxy this would correspond to $|\vec{v}| \leq 544 kms^{-1}$.

Assuming a collision-less gas of particles, the expected shape of the halo can be derived to be an isotropic and isothermal sphere with density profile $\rho \propto r^{-2}$. The velocity distribution in the galactic rest frame would thus follow a Maxwell-Boltzmann distribution* similar to,

$$\begin{aligned} f_{GAL}(|\vec{v}|) &= \frac{1}{\sqrt{2\pi}\sigma} \exp\left(-\frac{3|\vec{v}|^2}{2\sigma^2}\right) \\ \sigma &= \sqrt{\frac{3}{2}} v_c \end{aligned} \tag{2.3}$$

which depends on the local circular velocity in the galactic plane $v_c \approx 220 kms^{-1}$ [27]. It is also important to note that the velocity vectors would not have a preferential direction of motion making the global and local flux of particles entering or leaving the halo to be zero,

$$\sum_{\text{DM particle } i}^{Halo} \vec{v}_i^{GAL} \approx \vec{0}. \tag{2.4}$$

The local DM density with respect to the Earth's position in the galaxy can also be approximated using observational data on the galactic rotation. As derived in Reference [28], the

* Although unlikely to be absolutely accurate, this model is satisfactory for the purpose of this project. An interesting extension to this study can be conducted when considering alternative mass and velocity distribution models or even possibly a model-independent case.

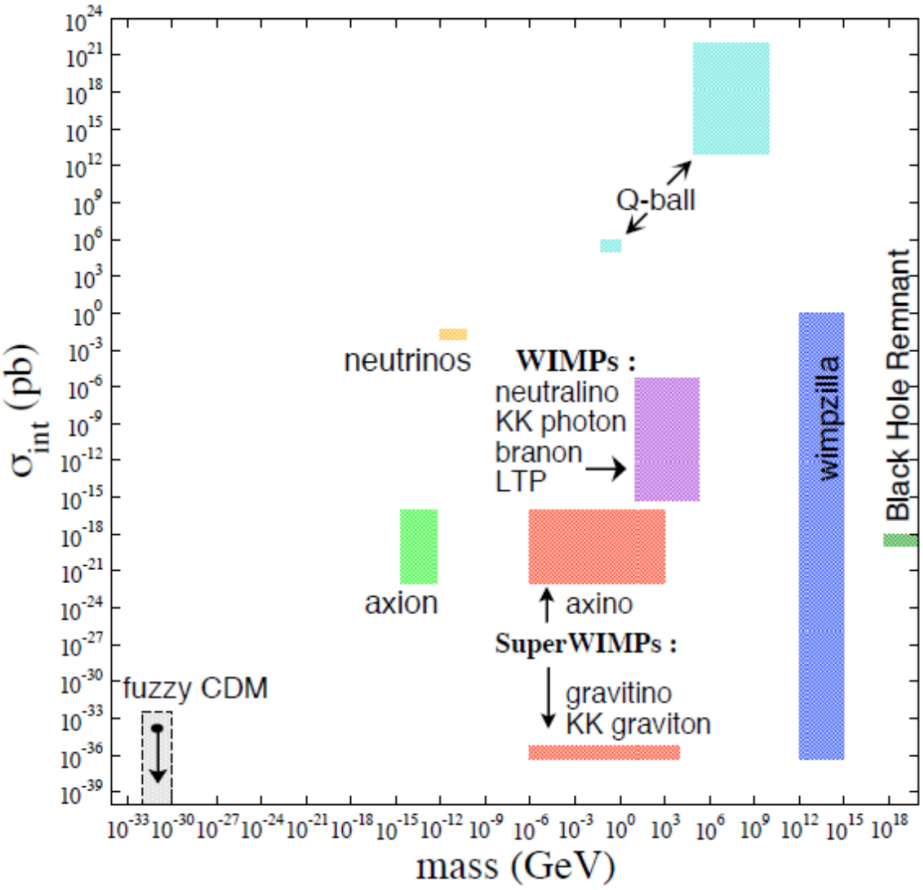

Figure 2.3. The logarithmic parameter space of mass against interaction cross-section of a variety of DM particle models. The candidates shown above do not necessarily take into account all relevant constraints or exclusions. For more information on the individual models and their current standing advise [23]. Image taken from Reference [26].

allowed range of the DM local density as is constrained by rotation curves for a range of halo profiles is $0.2-0.8\ GeVcm^{-3}$. For the purpose of this study, the local density in the galactic neighbourhood will be chosen to be $\rho_o = 0.3\ GeVc^{-2}cm^{-3}$ in accordance with results from Reference [29]. Even though the constraints on ρ_o are not narrow, this study will assume zero theoretical uncertainty on this value to produce highly model dependent results.

2.3.2 Local Frame of Reference

Perhaps the most important premise for this work is the fact that, from the frame of a terrestrial observer the distribution of incident DM particles will not be isotropic. Equations 2.3 & 2.4 describing the distribution of DM velocities in the galactic frame ought to be modified to describe the expected distribution observed in an earthbound Laboratory, moving through the galaxy and thus through the DM Halo. To do so, one must consider several frames of reference, all of which can be accurately approximated through Galilean transformations.

In the galactic frame, the sun, in addition to rotating around the galactic centre ($\vec{V}_{GalRev}$),

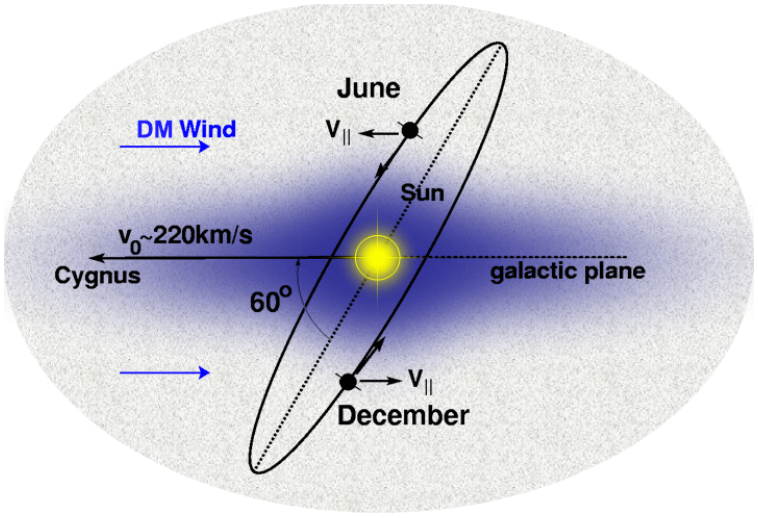

Figure 2.4. A visual representation of the relative motion of the earth in the galactic plane that gives rise to the DM wind and annual modulation effects. The Earth's revolution around the Sun is shown in its tilted pane with respect to the solar plane of revolution around the galactic centre. The local circular velocity is indicated as $v_0 \approx 220 kms^{-1}$ and the effective direction of motion, and thus the origin of the wind, aligns with the position of the Cygnus constellation. Image taken from Reference [33].

describes a procession within the rotation disk ($\vec{V}_{SolMot}$) [30, 31]. In turn, the earth rotating in a plane which is tilted 60^o with respect to the the galactic frame will define an elliptic path around the sun ($\vec{V}_{EarthRev}$) [32]. Finally, an observer placed on the surface of the earth will be moving with velocity ($\vec{V}_{EarthRot}$) around earth's axis of rotation with which in turn experiences an annual precession. The final component will depend on the geographical latitude of the observer.

$$\begin{aligned} \text{Galactic Revolution } & \left|\vec{V}_{GalRot}\right| \approx 220 kms^{-1} \\ \text{Solar Motion } & \left|\vec{V}_{SolMot}\right| \approx 18 kms^{-1} \\ \text{Earth's Revolution } & \left|\vec{V}_{EarthRev}\right| \approx 29 kms^{-1} \\ \text{Earth's Rotation}^* & \left|\vec{V}_{EarthRot}\right| \approx 0.3 kms^{-1} \\ \text{Combined Motion } & \left|\vec{V}_{Lab}\right| \approx 245 kms^{-1} \end{aligned} \tag{2.5}$$

The combined contributions to the DM velocity distribution in the laboratory frame is often referred to as DM *wind*, illustrated in Figure 2.4. A distinction needs to be made between Equation 2.3, which concerns the DM velocity distribution in the galactic rest frame, and the velocity distribution effectively relevant to an observer on the surface of the Earth.

The annual phase in the revolution of the Earth will give rise to a modulation in the expectation peak of the velocity distribution. This is due to the alignment (anti-alignment)

*This quantity was calculated for an observer located in Edinburgh.

of components in the relative motion of the Earth and Sun and gives rise to higher (lower) expected incident DM flux in June (December). In addition to this annual modulation, a daily modulation is expected to be observed with respect to the direction of origin of DM. As shown in Figure 2.4, the DM wind will coincide with the general direction of Cygnus and thus will move with the constellation as it moves in the sky above the Lab while the earth rotates.

2.3.3 WIMPs

Perhaps the most widely accepted of all the candidate models is the Weakly Interacting Massive Particle (WIMP). Generally defined by its weak or sub-weak interaction cross-section candidates this model accommodates particles whose mass is several to a few hundred GeV. The cross-section of such a particle can be expressed as

$$\langle \sigma v \rangle \approx \frac{g_{\text{weak}}^4}{16\pi^2 m_\chi^2}. \tag{2.6}$$

Substituting Equation 2.6 into Equation 2.2, reproduces a value for the relic density comparable to the observed. This *"coincidence"* is often referred to as the WIMP *miracle*.

Predictions of WIMP-like particles are found in several theoretical frameworks. An example of such would be the neutralino, part of R-parity conserving Supersymmetry [34]. The neutralino family is composed of four hypothetical neutral supersymmetric fermions, the lightest of which is stable and a prime WIMP candidate that ranges from $10 GeV$ to $10000 GeV$.

Through the supersymmetric models [35], interactions between the WIMP and target nucleus' quarks are expected to mediate via the exchange of either a squark or Higgs boson. The interaction Lagrangian contributing will contain the terms

$$\mathscr{L}_{SI} \supset \alpha_q^S \bar{\chi}\chi\bar{q}q + \alpha_q^V \bar{\chi}\gamma_\mu\chi\bar{q}\gamma^\mu q, \tag{2.7}$$

corresponding to scalar-scalar and vector-vector couplings respectively [27] . This scalar interaction will also receive contribution from WIMP-gluon scattering processes and the combined interaction is recast as a WIMP-nucleon interaction. To retrieve the WIMP-nucleus Scalar interaction matrix element and thus the Spin-Independent (SI) cross-section, the appropriate nuclear form factor needs to be taken into account [36, 37]. It should be noted that the above interaction couples to the target's mass and thus the nucleon number, favouring interactions with heavier elements.

Another important contribution to the interaction cross-section stems from the axial-vector-axial-vector couplings between the nucleon spin and the non-zero WIMP spin (Dirac or Majorana Fermion). The interaction Lagrangian, as derived in Reference [38], will contain terms of the form,

$$\mathscr{L}_{SD} \supset \alpha_q^A (\bar{\chi}\gamma^\mu\gamma_5\chi)\left(\bar{q}\gamma_\mu\gamma^5 q\right), \tag{2.8}$$

In the particular case, the WIMP-quark interaction has to be adjusted according to the appropriate nuclear spin Form Factor [39]. These Spin-Dependent (SD) interactions, even though smaller in contribution, can become significant for high spin nuclear targets.

2.4 Direct Detection

In the endeavour to identify the nature of DM, direct detection experiments have demonstrated leading contributions. In essence, large bodies of radio-clean target material are placed far underground, shielded from cosmic rays and radiation from the surroundings. The aim of this type of experiment is to directly measure energy deposits that rarely interacting particles leave in the detector as they pass through. Information about a scattering event can be harvested in any of the three forms: ionization of nuclei due to collision, scintillation light released during de-excitation of atoms, and propagation of phonons in cryogenic detectors [40].

Some properties of a material that become extremely advantageous in these types of searches are, high nuclear mass, low-radioactivity of isotopes, low ionisation threshold, transparency to scintillation light, conductivity, ease of collection and operation, and scalability. Liquid noble gas detectors have so far lead recent efforts in the exploration of new parameter space of DM models, with several multi ton experiments underway [41–46]. Because of the dense nature of the liquid targets, the active material is exceedingly self-shielding. In combination with high electron conductivity, low ionisation threshold, and scintillation light transparency, liquid noble gases are ideal for rare event searches.

2.4.1 Directional Detectors

Perhaps a different family of direct DM detection is the detectors that have the capability to extract information about the direction of impinging particles [47]. This has been accomplished through several technologies in the past. On one hand, extremely low pressure time projection chambers have been used to record the track of recoiling nuclei through ionisation paths [48]. With extremely low threshold energies $E_{th} \approx 20keV$ and the capability to resolve the drift tracks of the recoiling nuclei $\sim 50cm$, these type of detectors are viable. Reconstructing the recoiling nucleus, allows for the interpolation of the direction of origin of the incident particle. This allows for the observation of both daily and annual modulation as discussed in Section 2.3.2. However, having an operating pressure of a few $mbar$, the up-scaling potential of these experiments remains as one of the limiting challenges.

On the other hand, detectors can have directional sensitivity through their differential cross-section [49]. These types of detectors take advantage of broken symmetries in the material that affect the strength of interaction. Alignment of nuclear spins in a polarised detector will affect the spin dependent interactions whereas plane spacing in a crystal may cause constructive interference in bragg scattering. The latter has been hypothesised as a directional detection method for QCD Axions; a sub-GeV candidate for DM [50]. In this study, the effects of polarisation in DM detection are explored for Xenon, a material that has proven its worth in direct detection.

2.4.2 Polarised Frozen Xenon

Even though Xenon has been used in several DM direct detection experiments, its use as a detector target in a solid form and in a polarised state has not been attempted. With a freezing point at around $161K$, the operation temperature of such a detector would not be far from liquid

Xenon detectors.* Important properties of the frozen material is that it remains transparent to its own scintillation light, and conducts charge [51, 52]. Dual phase scintillation would thus still be achievable as it is implemented in the liquid detectors. Some concerns with the scalability of a target to a ton-scale are justifiable since ensuring uniformity across the crystal is hard to achieve [53].†

The polarisation of frozen Xenon has also been proven possible through several experiments [54, 55]. At a temperature of $77K$ the relaxation time of an approximately 50% polarised sample was measured to be 3 hours and at $4K$ the projected relaxation time is expected to be over 40 days. As cryogenic detector technologies improve, the feasibility of a detector collecting data at these temperatures is not unrealistic. ‡

2.5 Differential Rate Calculations

The theoretical framework that allows for a prediction of the expected total rate and frequency density of energy deposits in a direct detection experiment is the differential rate equation. Commonly expressed in units of $counts\ kg^{-1}\ day^{-1}\ keV^{-1}$, this spectrum can be integrated over a range of recoil energies defined by the specific detector's energy threshold to represent the total expected rate of events observed per day of data taking and kilogram of active material. It is computed as the product of the target's density, DM flux and differential cross-section integrated over all contributing DM velocities.

The flux is obtained through the product of the local particle number density ρ_o/m_χ, and the DM particle velocity v. However, due to the distribution of velocities of incident DM particles, the full spectrum of particles energetic enough to produce an interaction with a given E_{NR} needs to be accounted for. Since the interaction is rooted in the collision kinematics between an incoming DM particle and stationery nucleus, as is derived in the Appendix, Section A.1, the Recoil Energy E_{NR} as a function of the scattering angle θ is

$$E_{NR} = \frac{\mu_N^2 v^2}{m_N}(1-\cos\theta), \tag{2.9}$$

where the reduced mass of a DM particle m_χ and a target nucleus m_N is defined as $\mu_N = (m_N m_\chi)/(m_N + m_\chi)$. Due to the scattering angle dependence of Equation 2.9, a range of recoil energies is expected to be caused by an incident particle of a fixed velocity and vice-versa. A head-on collision, $\theta = \pi$ will thus represent the most energetic elastic recoil allowed with

$$v_{\min} = \sqrt{\frac{m_N E_{NR}}{2\mu_N^2}}. \tag{2.10}$$

The differential rate can be pieced together, following [56], as a function of the WIMP mass m_χ,

*Xenon's liquid phase is between 161K and 165K

†The mass of the largest successfully grown frozen Xenon crystal is $2kg$. [53]

‡If an operation temperature in the mK scale is chosen, the possibility for harvesting phonon scintillation from nuclear recoil events becomes accessible.

target nucleon mass m_N, local density ρ_o and differential cross-section $\frac{d\sigma}{dE_{NR}}$ to be

$$\frac{dR}{dE_{NR}} = \frac{\rho_o}{m_N m_\chi} \int_{v_{\min}}^{\infty} v f(v) \frac{d\sigma}{dE_{NR}}(v, E_{NR})\, dv. \tag{2.11}$$

The velocity distribution function has been introduced as a weight to the DM particle velocities and will play a very central role in this study as previously discussed. The differential cross-section contains the input from the physics of the particle interaction between the DM particle and the nucleus in the differential event rate. as discussed briefly in Section 2.3.3, a DM candidate is expected to scatter off the target nucleus via a combination of SI and SD exchange currents. This can be reflected by separating the interaction, in the two individual contributions,

$$\frac{d\sigma}{dE_{NR}} = \left(\frac{d\sigma}{dE_{NR}}\right)_{SI} + \left(\frac{d\sigma}{dE_{NR}}\right)_{SD}. \tag{2.12}$$

2.5.1 Spin Independent Rate

For the SI, the velocity and energy dependence of the cross-section can be separated by writing

$$\left(\frac{d\sigma}{dE_{NR}}\right)_{SI} = \frac{m_N \sigma_0 F_{SI}^2(E_{NR})}{2\mu_N^2 v^2}, \tag{2.13}$$

following [27]. In the equation above, the Form Factors F_{SI}^2 represents the Fourier transform of the nucleon density and reflects the loss of coherence as a function of increasing momentum transfer. A common parametrisation with respect to the momentum transfer $q = \sqrt{2 m_N E_{NR}}$ is

$$F_{SI}^2(q) = \left(\frac{3 j_1(qR_1)}{qR_1}\right)^2 \exp\left(-q^2 s^2\right), \tag{2.14}$$

where j_1 is s spherical Besel function. Parameters $s \approx 1 fm$ and $R_1 = \sqrt{R^2 - 5s^2}$ describe the size and form of the nucleus, where $R \approx 1.2\sqrt{A} fm$ with A being the mass number of the target nucleus. Finally the fundamental cross-section σ_o can be expressed as a function of the coupling of DM to protons and neutrons. While taking the approximation for an identical WIMP-proton and WIMP-neutron coupling then

$$\sigma_0 = A^2 \frac{\mu_N^2}{\mu_p^2} \sigma_p^{SI}, \tag{2.15}$$

where $\mu_p = (m_p m_\chi)/(m_p + m_\chi)$ for nucleon mass m_p. Combining Equations 2.11, 2.13 and 2.15 the SI differential rate is shown to be,

$$\left(\frac{dR}{dE_{NR}}\right)_{SI} = \frac{\rho_o A^2}{2\mu_p^2 m_\chi} \sigma_p^{SI} F_{SI}^2(E_{NR}) \int_{v_{\min}}^{\infty} \frac{f(v)}{v} dv. \tag{2.16}$$

2.5.2 Spin Dependent Rate

A similar breakdown of the SD cross-section in the q parametrisation will yield,

$$\left(\frac{d\sigma}{dq^2}\right)_{SD} = \frac{\sigma_0}{4\mu_N^2 v^2}\frac{S_A(q)}{S_A(0)}, \tag{2.17}$$

where S_A is the Spin Structure function, analogous to the nuclear form factor and obtained through nuclear shell calculations [39]. The specific coupling to the individual nucleons will have to be expressed as

$$\sigma_{p,n}^{SD} = \frac{3\mu_{p,n}^2(2J+1)}{4\pi\mu_N^2}\frac{\sigma_0^{SD}}{S_A(0)}, \tag{2.18}$$

where J is the total nucleus spin, and$\mu_{p,n}$ is the reduced mass with respect to the proton and the neutron respectively. It is important to note that, in contrast to the SI case, there is no A^2 factor contributing to the SD cross-section. In addition, due to the J dependence, targets with higher nuclear spin will demonstrate stronger SD contributions. Combining Equations 2.11, 2.17 and 2.18, the SD differential rate, following [57], can be derived to be*,

$$\left(\frac{dR}{dE_{NR}}\right)_{SD} = \frac{\rho_o}{3\mu_{p,n}^2 m_\chi (2J+1)}\sigma_{p,n}^{SD} S_A^2(E_{NR})\int_{v_{\min}}^{\infty}\frac{f(v)}{v}dv. \tag{2.19}$$

2.6 Exclusion Plots and the Neutrino Floor

Given the DM signal spectra predictions, i.e. 2.16 and 2.19 the relevant parameter space shown in 2.3 can be explored. The total target mass and the length of data collection defines the number of DM signal events expected. Good understanding of the detector response through calibrations in combination with a complete background model in the relevant energies allows for the separation of the collected data in signal and background events. If no events are recorded that lie in the signal region of a given mass-cross-section combination, then that region of parameter space can be excluded with a given degree of confidence. Longer runs and heavier targets allow for smaller cross-sections to become accessible. Lighter target nuclei with different nuclear form-factors and spin components, allow for wider resolution due to the differences in the differential rate. An example exclusion plot for WIMPs with limits from several experiments is shown in Figure 2.5.

One of the most important aspects in the success of direct detection experiments is their ability to find a space where the recorded nuclear recoil energy signatures caused by DM candidates can be separated from the signatures due to background events. Given a combination of the signal harvesting methods described in Section 2.4 this can be achieved for the main source of background in the regions of interest. i.e. gamma rays and neutrons. This is essentially due to the difference in the physical interaction taking place. Most of the background will not undergo the same neutral-current interactions characteristic to a DM elastic scatter event. However, it is expected that given extremely low cross-sections a neutrino-nucleus coherent scattering event

*Note the parameter change from Equation 2.17 and 2.18 $q \rightarrow E_{NR}$

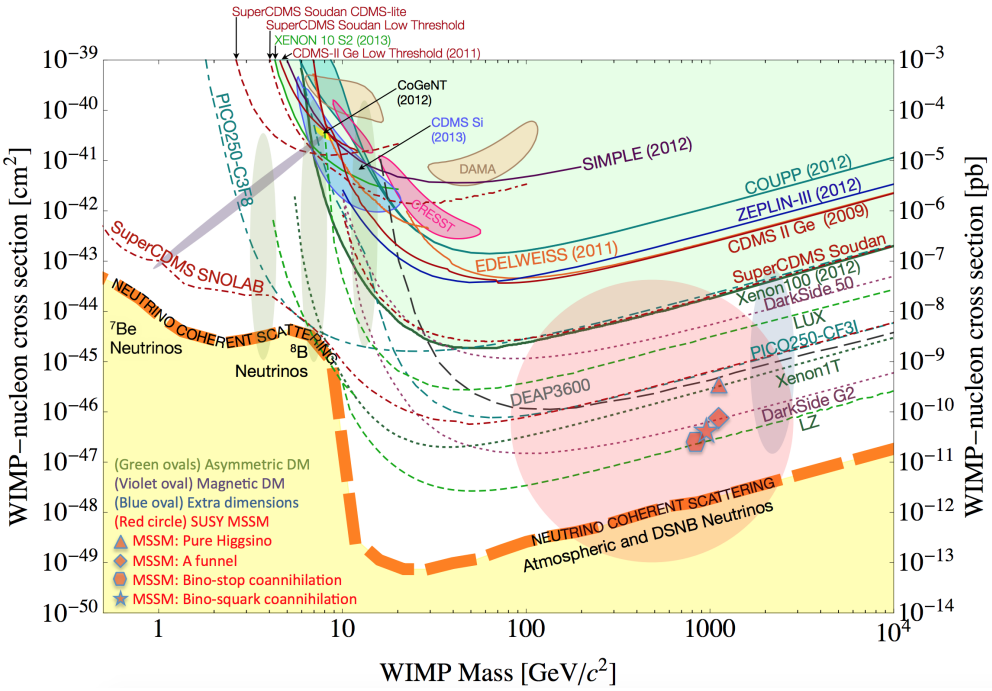

Figure 2.5. Plotted in the space of WIMP-nucleon interaction cross-section and WIMP mass, the SI cross-section limits are presented for a series of experiments (solid curves). Parameter space above each limit is excluded. The projected limits expected to be set through future experiments are also shown (dashed curves). Potential signatures seen by individual experiments are shown in bound shaded areas whereas favoured models are shown in un-bound shaded regions and symbols. The neutrino floor is also projected in yellow. [58].

will interfere with the discrimination capabilities of direct detection experiments due to the similarity between the scattering processes.

The parameter space affected, often referred to as *neutrino floor* and shown in Figure 2.5, is not yet accessible by the experiments currently running but is expected to be present in data collected in the next decade. The importance of the observation of the neutrino floor is twofold. Other than confirming a previously unobserved physical interaction predicted by the standard model [59], it will also signify final boundaries of this generation of direct detection experiments [60]. First evidence of the neutrino floor be in the form of detector signatures that resemble a $6GeVc^{-2}$ WIMP but will in fact be caused through a neutral-current interaction event due to a Solar ^{8}B neutrino. The aim of this study is to use the properties of a polarised Xenon detector in the discrimination of signal and background in the neutrino floor.

3 Methods

The study that follows was based on a Monte-Carlo algorithm that was specifically designed and developed to produce virtual DM and solar neutrino spectra. The main focus was split between the generation of velocity-vectors (direction and amplitude) according to user specified

distributions, and establishing the infrastructure for frame of reference manipulation. Both the simulation and analysis software were written and compiled in C++11 while implementing ROOT6 Libraries [61] for data handling and plotting. Object oriented structure was adopted to facilitate future modifications and extensions to the software.

3.1 Particle Generation

To study the differences in the incident DM and neutrino particles as they are observed, a Monte-Carlo algorithm assigns particles with momentum vectors. Data was generated for a uniformly distributed selection of days in the year, as well as hours in the day. To take advantage of the information on directionality that is encoded in the particle velocities generated, individual collision kinematics were simulated, assigning angle of scatter and recoil energy to each particle interaction with the target nuclei. This was then converted into an effective differential rate through averaging over the required quantities.

3.1.1 Dark Matter Wind

To fully describe the DM wind, three nested frames of reference were implemented in descending scale: galactic, equatorial and laboratory frames. The formalism that was implemented in this section follows the derivation from Reference [6].

- The Galactic frame is defined with its origin at the position of the Sun. The three axes $(\hat{x}_g, \hat{y}_g, \hat{z}_g)$ are oriented such that $\hat{x}_g$ points to the galactic centre, $\hat{y}_g$ points towards the direction of galactic rotation, and $\hat{z}_g$ points to the North galactic pole.

- The Equatorial frame, often referred to as the Geocentric Equatorial Inertial frame, is defined to have its origin at the centre of the Earth. From its axes $(\hat{x}_e, \hat{y}_e, \hat{z}_e)$, $\hat{z}_e$ is placed to be parallel to the Earth's axis of rotation and points to the North Celestial Pole, $\hat{x}_e$ points towards the vernal equinox, and $\hat{y}_e$ is placed on the celestial equator such that a right-handed Cartesian frame is formed.

- The Laboratory frame, is defined to rest on the surface of the Earth with axes $(\hat{\mathcal{N}}, \hat{\mathcal{W}}, \hat{\mathcal{Z}})$. $\hat{\mathcal{N}}$ and $\hat{\mathcal{W}}$ points towards geographical North and West respectively, whereas $\hat{\mathcal{Z}}$ points in the direction of the Zenith, radially away from the centre of the Earth.

Since the relative position and velocity of these frames experiences temporal and spacial dependence of the observer, customary parametrisation was adopted. This includes definitions of the Local Apparent Sidereal Time t_{Lab}, and the Sun's ecliptic longitude $\lambda(t)$. The exact expressions implemented in this study are presented in the Appendix, Section B. As briefly mentioned in Section 2.3.2, the relevant velocities that were considered are as follows.

- Galactic rotation, defined in the galactic frame as the local circular velocity has been fixed according to [30] as

$$\vec{V}_{GalRot} = 220\ \hat{y}_g\ kms^{-1} \tag{3.1}$$

- Solar motion, defined in the galactic frame as [31]

$$\vec{V}_{SolMot} = \left(11.1\ \hat{x}_g + 12.2\ \hat{y}_g + 7.3\ \hat{z}_g\right) kms^{-1} \tag{3.2}$$

- Earth's revolution, defined in the galactic frame as [62],

$$\begin{aligned}\vec{V}_{EarthRev}(t) = V_{\oplus}(\lambda(t))\,[\,&\cos\beta_x \sin\left(\lambda(t)-\lambda_x\right)\ \hat{x}_g \\ &+ \cos\beta_y \sin\left(\lambda(t)-\lambda_y\right)\ \hat{y}_g \\ &+ \cos\beta_z \sin\left(\lambda(t)-\lambda_z\right)\ \hat{z}_g\ ],\end{aligned} \tag{3.3}$$

  where $V_{\oplus} = 29.8\ kms^{-1}$ is the average orbital speed of the Earth, adjusted for the ecliptic nature of the orbit $V_{\oplus}(\lambda(t)) = V_{\oplus}[1-0.016722\sin(\lambda(t)-14^o)]$. In addition, factors $\beta_i = (-5^o.5303, 59^o.575, 29^o.812)$ and $\lambda_i = (266^o.141, -136^o.3485, 179^o.3212)$, account for the ecliptic latitude and longitude adjustments necessary to describe an orbit tilted with respect to the galactic rotation plane.

- Earth's rotation, defined in the laboratory frame for convenience,

$$\vec{V}_{EarthRot} = -V_{RotEq}\cos(\lambda_{Lab})\ \hat{W} \tag{3.4}$$

  where $V_{RotEq} = 0.465102$ is the speed of rotation at the Equator, and λ_{Lab} is the geographical latitude of the lab.

The effective velocity of the Lab with respect to the galactic rest frame, that is the cause of the expected DM wind is defined as the sum of the relative velocities. The wind direction of incidence can thus be expressed as,

$$\vec{V}_{Wind}(t) = -\left[T_{\mathrm{Equ}\to\mathrm{Lab}}(t)\,T_{\mathrm{Gal}\to\mathrm{Equ}}\left(\vec{V}_{GalRot} + \vec{V}_{SolMot} + \vec{V}_{EarthRev}(t)\right) + \vec{V}_{EarthRot}\right], \tag{3.5}$$

where $T_{\mathrm{Equ}\to\mathrm{Lab}}$ and $T_{\mathrm{Gal}\to\mathrm{Equ}}$ are frame of reference transformation matrices, defined in detail in the Appendix, Section B.2. Note that for the scale of this study, $T_{\mathrm{Gal}\to\mathrm{Equ}}$, is effectively a constant and thus is assumed to have no temporal dependencies.

In this study, a laboratory located in the Physics Building of the University of Edinburgh was chosen with latitude $\lambda_{Lab} = 55^o.921731$ and longitude $l_{Lab} = -3^o.174090$. Verification of the output was conducted through the use of planetary simulation software, Stellarium*. The altitude and azimuth of the Cygnus constellation as presented in Stellarium for a given date, time and observer location was confirmed to be in the effective direction of incidence of the calculated DM wind $-\vec{V}_{Wind}$.

At this stage, the effects of DM wind in the speed distribution of DM particles in the laboratory frame can be demonstrated. The function shown in Equation 2.3 was sampled to generate spectrum of DM particle speeds. Each generated speed is then associated with a spherically isotropically distributed direction vector in the galactic frame. These vectors representing

*www.stellarium.org/

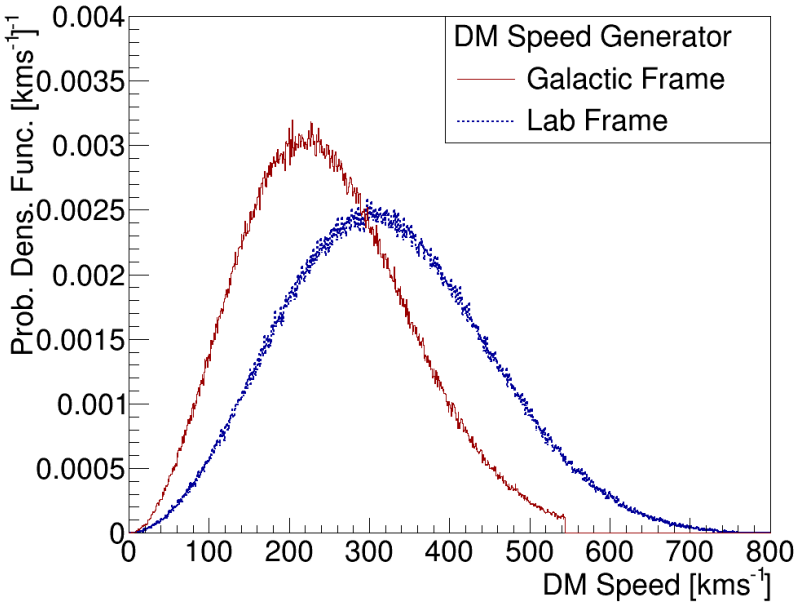

Figure 3.1. Generated velocity distribution PDFs for galactic & laboratory frame of reference. The velocity distribution in the galactic frame was suppressed to zero beyond the escape velocity $v_{Esc} = 544$ in agreement with a bound galactic halo.

the DM velocities can be transformed to the laboratory frame via a linear shift* defined in Equation 3.5. Figure 3.1 shows the Monte-Carlo generated probability-density function of the DM velocity vector magnitudes in the two relevant frames. In addition Figure 3.2, shows the amplitude of the annual modulation of the DM wind. This modulation is also in agreement with what is shown in Figure 2.4, higher (lower) overall DM velocities experienced in June (December).

3.1.2 Solar Neutrinos

The neutrino background relevant to DM direct detection experiments receives several contributions from solar, atmospheric, and diffuse supernovae, sources. The area of interest to this study is the area where the neutrino floor interferes with the discovery potential of direct detection. Identifying this from Figure 2.5, ^{8}B solar neutrinos are of primary interest. Produced in fusion processes in the Sun, ^{8}B neutrinos will only constitute approximately 0.02% of the total flux and depend strongly on the particular metallicity model chosen. Having assumed a high metallicity Standard Solar Model,† the absolute normalisation of the flux has been constrained by the recent results of the Borexino experiment [64] to be,

$$\Phi_0^{^8B} = 5.58(1 \pm 0.14)\ 10^6\ cm^{-2}s^{-1} \tag{3.6}$$

*This step takes advantage of the spherically symmetric nature of the DM vector distribution in the galactic frame. Any frame rotated around any axis with respect to the galactic frame would describe an equivalent DM galactic direction vector distribution and the shift described in Equation 3.5 can be applied linearly to describe the distribution in the laboratory frame.

†As it remains consistent with SNO neutral-current measurements [63].

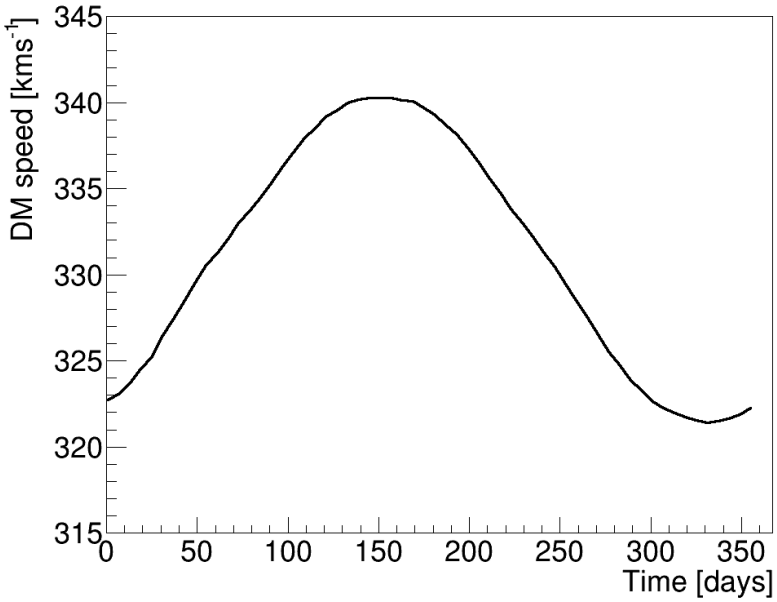

Figure 3.2. Modulation evident in the average speed for the Monte-Carlo generated DM particles shifted to the laboratory frame. This can also be interpreted as the mean of the shifted velocity density distribution (blue line) shown in Figure 3.1. The maximal (minimal) value, located at approximately day 150 (330) corresponds to the month of June (December) during which the velocities of the Sun and Earth add constructively (destructively).

Furthermore, to incorporate the ellipticity of the orbit of the earth, and the modulation in the radial distance from the sun, Equation 3.6 needs to be modified to,

$$\Phi^{\nu}(t_d) = \Phi_0^{\nu}\left[1 + 2\epsilon\cos\left(2\pi\frac{t_d - 3}{365}\right)\right]. \tag{3.7}$$

This includes the eccentricity of orbit,$\epsilon = 0.016722$ as a measure of the amplitude of the modulation, and is defined as function of time in the unit of days, t_d. The percentile amplitude modulation is approximately $\pm 3\%$.

The specific energy distribution was taken from Reference [65] and the spectrum, as sampled by the Monte-Carlo algorithm is displayed in Figure 3.3. The direction of origin was taken to be identical for all solar neutrinos and set to be overlapping with the centre of the position of the Sun with respect to the observer. The details of the algorithm implemented for obtaining the position of Sun in the equatorial frame is outlined in the Appendix, Section B.3. The direction of origin for solar neutrinos was thus set to be,

$$\hat{V}_{\nu}(t) = -T_{\mathrm{Equ}\rightarrow\mathrm{Lab}}(t)\hat{R}^{Eq}_{Sun}(t). \tag{3.8}$$

3.1.3 Expectation Value calculations

The generated particle data are used for the determination of expectation values necessary for the calculation of the theoretical rate spectra. As an example, to obtain the standard SI differential

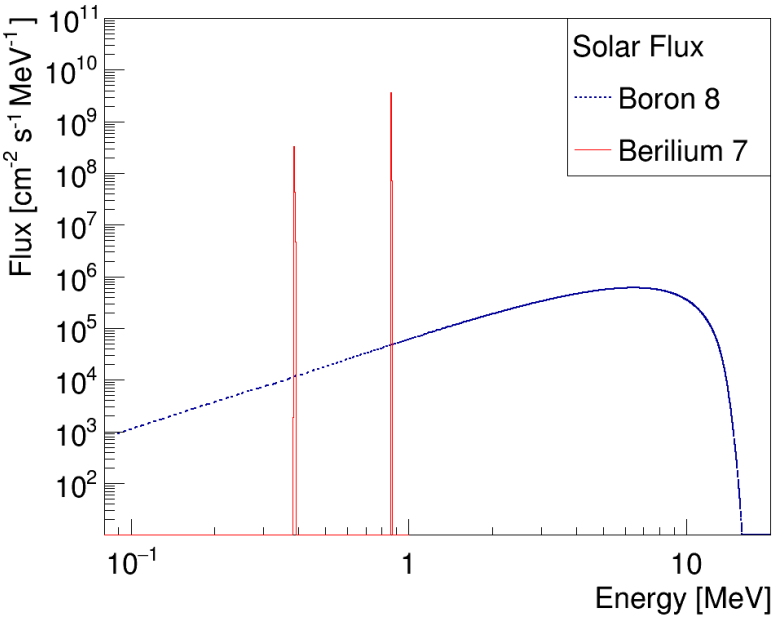

Figure 3.3. The above figure displays the solar neutrino spectra currently integrated in the neutrino energy generation, normalised to the absolute flux. This does not include the error in the normalisation as the error bars would not be visible in this scale. The two peaks from ^{7}Beryllium correspond to $384keV$ and $862keV$.

rate for a sample of generated WIMPs, as shown in Equation 2.16, the expectation value of the inverse velocity magnitude is required. To satisfy the lower boundary condition, v_{min}, of the integral, the samples are filtered before averaging. The weight of the accepted particles with respect to the full sample will scale the sum, acting as a probability density, such that,

$$\Xi[f(v),E_{NR}] = \int_{v_{\min}}^{\infty} \frac{f(v)}{v} dv = \frac{n_c}{N}\left(\frac{1}{n_c}\sum_{i=0}^{n_c}\frac{1}{|\vec{v}_i|}\right) = \frac{1}{N}\sum_{i=0}^{n_c}\frac{1}{|\vec{v}_i|} = \left\langle\frac{1}{v_c}\right\rangle. \tag{3.9}$$

In the Equation above, the sum is carried over the total number of particles n_c that satisfy the condition $v_i > v_{min}$. The error of the mean is calculated through first obtaining the weighted sample mean variance,

$$\sigma^2 = \frac{n_c}{N}\left(\frac{1}{n_c}\sum_{i=0}^{n_c}\left(\frac{1}{|\vec{v}_i|} - \left\langle\frac{1}{v_c}\right\rangle\right)^2\right) = \frac{1}{N}\sum_{i=0}^{n_c}\left(\frac{1}{|\vec{v}_i|} - \left\langle\frac{1}{v_c}\right\rangle\right)^2, \tag{3.10}$$

and then calculating the standard deviation using $\sigma/\sqrt{n_c}$. The final statistical uncertainty in the integral will be,

$$\delta\Xi = \sqrt{\frac{1}{Nn_c}\sum_{i=0}^{n_c}\left(\frac{1}{|\vec{v}_i|} - \left\langle\frac{1}{v_c}\right\rangle\right)^2}. \tag{3.11}$$

For highly constraint theoretical models on velocity distributions this uncertainty will dominate in the order of 10^6 generated particles.

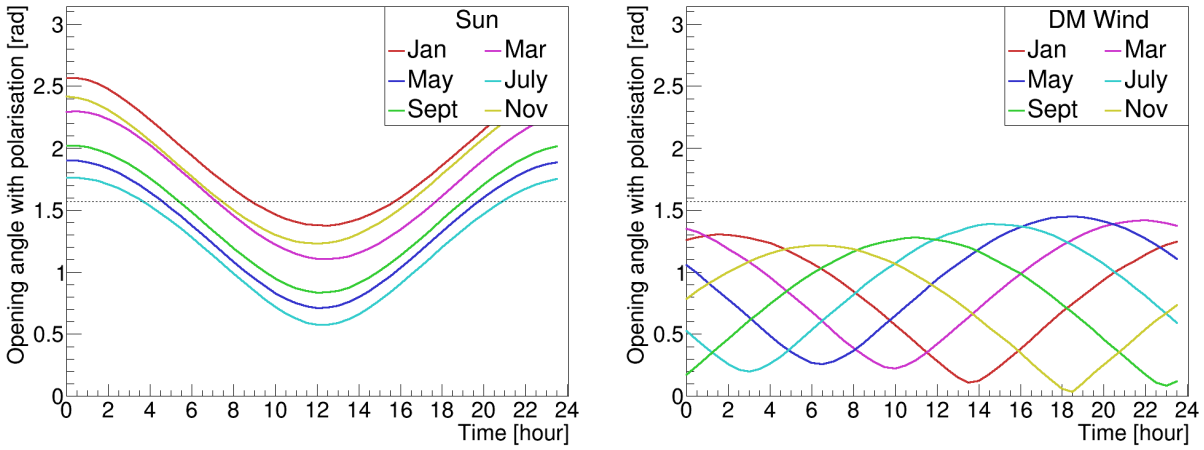

Figure 3.4. The y-axis of the above two figures presents the opening angle between the direction of origin of solar neutrinos (left) and DM wind (right) with respect to a polarisation vector pointing to the Zenith in the laboratory frame $(0,0,1)_{Lab}$. This angle is plotted against the time of day for the first day of each month and a laboratory latitude $\lambda_{Lab} = 55^{o}.921731$ and longitude $l_{Lab} = -3^{o}.174090$. With a dotted line the angle corresponding to a point on the horizon is also presented.

3.1.4 Directional differences

Given the directional characteristics of incident DM particles and solar neutrinos outlined in the previous two Sections, the differences in the effective direction of incidence can become evident. On a qualitative level, a visual representation of the incident DM particle density can be plotted for a two dimensional space spanning the sky above the laboratory. Parametrised with the altitude and azimuth of points on a spherical shell surrounding the observer, these density maps, as shown in Figures C.1 and C.2 of Appendix C, can be used to track the peak in incident DM particles in relation to the position of the Sun.

Perhaps a more quantitative way to demonstrate the distinction in the directionality is to study the opening angle between the expected direction of incidence and a fixed vector in the laboratory frame. Figure 3.4, shows the evolution of such an opening angle for the effective direction of origin of DM particles $-\vec{V}_{Wind}$, and for the position of the Sun $-\hat{V}_{\nu}(t)$. In addition to serving as further confirmation on the accuracy of the generated directional information, Figure 3.4 demonstrates the preservation of the uniqueness of the two functions throughout a calendar year.

3.2 Polarised Target Differential Rate

To conduct the investigation of how a polarised target would improve the detection capabilities of direct detection experiments, angular differential rate calculations were implemented for the neutrino background. In reality, the effects of the neutrino floor exists in both the SD and SI exclusion calculations, however the cross-section of the relevant neutrino interaction is 10 orders of magnitude smaller than current limits[57]. For this reason, the SD WIMP interaction rate is not considered in any further parts of this study.

3.2.1 Neutrino-Nucleus Coherent Scattering

Neutrinos are capable of depositing energy in a direct DM detector through either a neutral-current elastic scattering event with an electron or through a coherent neutral-current elastic scattering event with a target nucleus. The former, with a cross-section of $10^{-44} cm^2$ produces recoil energies of up-to few hundred keV and is easily filtered out during the separation of nuclear from electron recoil events in the parameter space of the collected signal. As mentioned earlier, the latter process, with a cross-section of approximately $10^{-39} cm^2$ has never been observed but is predicted and well understood through the Standard Model [66]. Coherence corresponds to the *"simultaneous"* interaction of the scattered neutrino with the nucleons of the target particle and occurs when the wavelength of the neutrino's momentum is of the order of the size of the nucleus. The constructive interference will cause an enhancement in the cross-section equal to $\left[N-\left(1-4\sin^2\theta_W\right)Z\right]$, where θ_W is the weak mixing angle, and Z and N are the number of target protons and neutrons respectively.

A decomposition of the interaction cross-section, as was introduced in References [66, 67], was conducted in reference [5] and the differential cross-section for a polarised nucleus was derived for neutrinos. The derivation of the expression is beyond the scope of this project, however its implementation was central to this study. Shown in its full functional form in the Appendix, Equation D.1, it contains SI and SD contributions. In analogy with Equation 2.9 the SI component depends on the scattering angle ψ between incoming and outgoing particles. The SD component scales as the number of unpaired nucleons in the target and presents dependence on the projection of incoming and outgoing velocities on the polarisation vector, $\hat{v}_\nu.\hat{s}_N$ and $\hat{v'}_\nu.\hat{s}_N$ respectively.

As the individual particle velocities before and after the recoil are generated and stored, the temporal dependence of the cross-section can now be taken advantage of. The differential rate for this interaction can then be expressed, in analogy with Equation 2.11 as,

$$\frac{dR_\nu}{dE_{NR}}(t) = n_T \int_{E_\nu^{min}}^{\infty} \Phi(E_\nu, t) \frac{d\sigma_{pol.}}{dE_{NR}}(E_\nu, t) dE_\nu, \tag{3.12}$$

where n_T is defined as the total number of target nuclei* and $\Phi(E_\nu, t)$ is the neutrino flux as discussed in Section 3.1.2.

4 Results and Discussion

The results are presented purely from an idealistic point of view such that the capabilities of a polarised detector can be explored on a theoretical level. The target material was assumed to be composed of 100% polarised Frozen Xenon that experiences no relaxation. In addition, the full mass of the target was considered to be pure ^{131}Xe; a stable Xenon isotope with nuclear spin $^3/_2$. The direction of polarisation was chosen to be in the vertical direction in the laboratory frame pointing towards the zenith. Differential rates are presented with respect to the corresponding nuclear recoil energy and a uniform detector efficiency is chosen at 50% acceptance.

*This quantity depends on Avogadro's number and the molar mass of the target material, expressed in appropriate units.

For the DM WIMP, Equation 2.16 was calculated using the generated particle information. A mass of 6 GeV was selected since it is one of the first masses to become inaccessible, as shown in Figure 2.5. The local DM halo density was set to be $\rho_o = 0.3\ GeVc^{-2}cm^{-3}$ with no associated uncertainty, and the velocity distribution of particles in the halo follows Equation 2.3. Velocity vectors in the galactic frame were then shifted to the laboratory frame according to the relative motion of the Earth, as derived in Equation 3.5. The nucleon interaction cross-section was set to be $\sigma_0 = 7\times10^{-45}cm^2$ corresponding to the border of the neutrino floor with currently accessible parameter space. If a distinction can be made at the level of this example, this would imply a detector capability that allows for the exploration of parameter space previously unreachable by direct detection experiments.

The differential rate for the solar ^{8}B neutrino were also calculated using Monte-Carlo generated directional and energy spectra. The direction of incidence was generated using the position of the Sun, shown in 3.8 whereas the energy spectra were implemented as shown in Figure 3.3. The absolute ^{8}B flux was set to be $\Phi_0^{^8B} = 5.58(1\pm0.14)\ 10^6\ cm^{-2}s^{-1}$ and the annual modulation shown in Equation 3.7 was also applied. Note that even though statistical uncertainties were calculated, the uncertainty on the absolute flux will dominate.

The plots included in this section are generated using a sample size of 10^6 for each particle. To study the hourly effects in the length of a chosen day, the temporal iterations were set to be of size 0.5 hours. For the annual scale, iterations of size 6 days were chosen for a 365-day year while the hour remained fixed.

4.1 Confirming the Effects of the Neutrino Floor

As a form of validation, the position of the neutrino floor has been reproduced as would be observed for this material, averaged over the temporal effect. The differential rate calculations, as shown in Figure 4.1, demonstrate the indistinguishability of the signal and background spectra with respect to recoil energy. Since the maximum recoil energy in this spectrum is observed at approximately $4keV$, the threshold energy of the detector has to be equal to or below $1keV$ for above energy range to be sampled. Threshold energies of keV and sub-keV have already been proven achievable in the case of the SuperCDMS experiment [68], however liquid noble gas experiments usually set an energy threshold of of a few keV. Any WIMP-nucleon interaction cross-section below the value of $7\times10^{-45}cm^2$ will be drowned in solar neutrino events. In addition, from approximately $\sigma_0 = 4\times10^{-45}cm^2$ the theoretical predicted WIMP rate will be smaller than the error bar width of the neutrino floor. A WIMP event recorded can and will be mistaken as being part of the background.

4.2 Daily modulation

Taking advantage of the angular effects in the differential cross-section of the neutrino background, a study was conducted with respect to the integrated event rate. Events with nuclear recoils between $1keV$ and $3keV$ were integrated and plotted for the length of a single day*. Since the angle of incidence of solar neutrinos with respect to the polarisation vector changes in

*The day chosen for this analysis was the 1st of March 2017 as the DM and neutrino flux are close to their average value and not in their extrema.

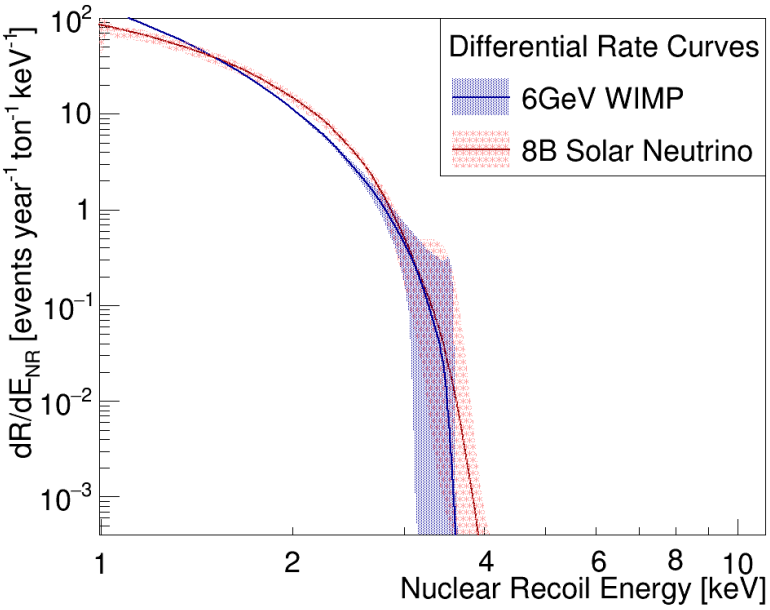

Figure 4.1. The differential rates are plotted for a pure ^{131}Xe target with a 50% nuclear recoil event acceptance, uniform across the recoil energy spectrum. Plotted in blue is the differential rate of a $6GeV$ DM WIMP acquired through a SI differential cross-section and a nucleon coupling strength $\sigma_0 = 7 \times 10^{-45} cm^2$. In red the differential rate for coherent scattering events of ^{8}B neutrinos. The uncertainty in the absolute flux of ^{8}B neutrinos is included in its differential rate as it is strongly contributing, both include the statistical uncertainty in the numerical integrations performed over the generated particle samples. At higher nuclear recoil energy both curves experience a large increase in their uncertainty caused by the relatively smaller number of high energy events generated. A direct comparison can be conducted between this plot and Figure 3 from Reference [69].

the length of a day, as shown in Figure 3.4, a modulation in the neutrino background is expected to be observed. The calculated neutrino rate is plotted on the left plot of Figure 4.2 along side the SI WIMP rate and modulation is indeed observed.

The combined rates shown on the right of Figure 4.2 clearly indicate how no features of the modulation are theoretically present for this detector. This is exclusively due to the size of the amplitude of the neutrino rate modulation being an order of magnitude smaller than the dominant error bar. If the features were more prominent, requiring a null hypothesis of modulating neutrino background with amplitude outside the one sigma error bar of the (flatter) combined rate, discrimination would have been possible.

Since the modulation amplitude in the hourly rates is effectively proportional to the number of unpaired nucleons, target nuclei of higher nuclear spin will experience larger amplitudes and may be able to produce theoretically achievable features in the daily rates. Amongst others, ^{73}Ge (nuclear spin of $^9/_2$) would be an ideal alternative candidate. In higher spin materials the SD cross-section for the WIMP-nucleon interactions becomes relevant and an angular decomposition of the WIMP SD cross-section may contribute strongly to modulation effects. However, it is now evident that the polarisation of a Xenon target will not enhance its discrimination capabilities.

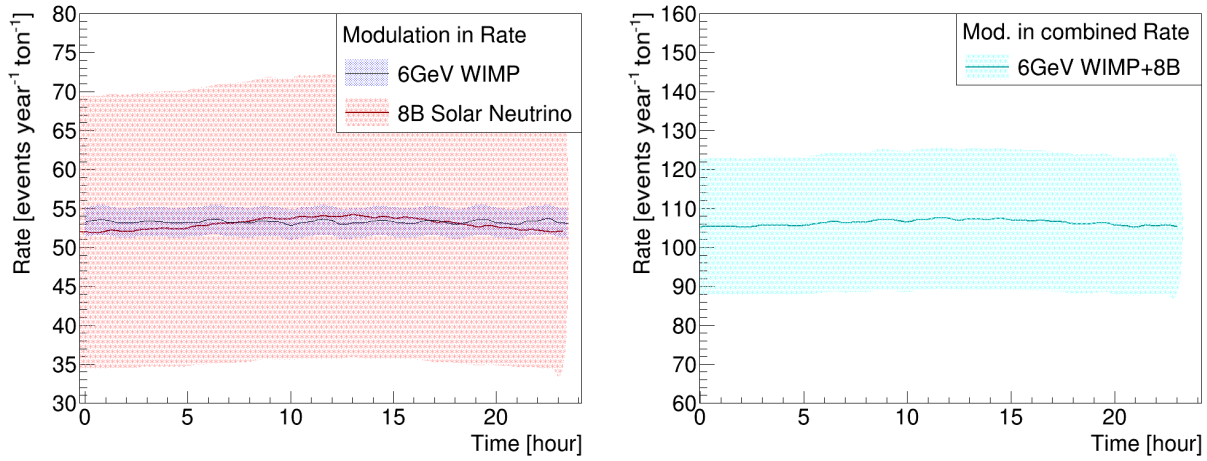

Figure 4.2. In the above two plots, the overlapping (left) and combined (right) theoretical differential rates for a $6GeV$ WIMP NR signal with $\sigma_0 = 7 \times 10^{-45} cm^2$ and a ^{8}B neutrino are plotted for different times in a day. The WIMP error bars do not contain any theoretical uncertainties and are dominated by the statistical uncertainties of the code. The neutrino error bars are dominated by the absolute flux uncertainty.

4.3 Annual modulation

Having demonstrated the insignificance of angular effects in the total rates due to polarisation, an attempt in discriminating the neutrino background from a WIMP signal through modulation in the annual flux of the individual sources is performed. Integrating over nuclear recoils between $1keV$ and $3keV$ the calculated rates are shown in Figure 4.3 for the year 2017. In the individual cases, the peak in the DM WIMP rate corresponds to higher DM wind velocities whereas the peak in the neutrino rate corresponds to the periapsis of the orbit of the Earh around the Sun. It is important to note that the null hypothesis is out of phase with respect to the WIMP signal. However, since the error in the combined rate covers a 20% range, well above the 7% modulation in the null hypothesis, discrimination in the phase between background and signal is not possible.*

5 Conclusion

Through the implementation of sophisticated algorithms, particle generation software was implemented to study the signal and background differential rate modulation of a polarised frozen Xenon direct DM detector. Having assumed an idealised 100% polarised isotopically pure ^{131}Xe detector the theoretical discrimination capabilities were tested in a daily and annual scale. The parameter space of interest was chosen to be the space where direct DM detection experiment meet the ^{8}B neutrino-nucleus coherent neutral-current background. The WIMP SI differential rate for a $6GeV$ particle with interaction cross-section of $\sigma_0 = 7 \times 10^{-45} cm^2$ was compared to

*Higher WIMP interaction cross-sections would have allowed for a larger modulation amplitude and thus the possibility of discrimination.

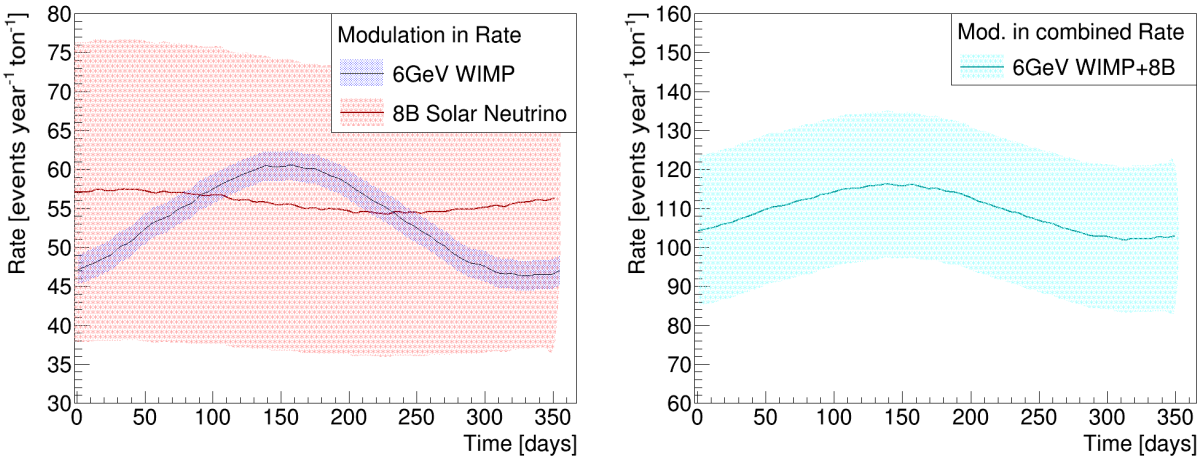

Figure 4.3. In the above two plots, the overlapping (left) and combined (right) theoretical differential rates for a $6GeV$ WIMP NR signal with $\sigma_0 = 7 \times 10^{-45} cm^2$ and a ^{8}B neutrino are plotted for different days in a year. The WIMP error bars do not contain any theoretical uncertainties and are dominated by the statistical uncertainties of the code. The neutrino error bars are dominated by the absolute flux uncertainty.

the angular differential rate for a ^{8}B solar neutrino. Having assumed minimal theoretical uncertainties in the velocity distribution and local particle density of DM, the uncertainty in the WIMP differential rate was assumed to be dominated by the statistical uncertainty within the generated data. The ^{8}B neutrino rate uncertainty being dominated by the uncertainty in the absolute solar neutrino flux was proven to be problematic.

In the scale of a day it was shown that the magnitude of the modulation present in the rate of ^{8}B solar neutrinos is one order of magnitude smaller than the uncertainty on the rate. The polarisation of this material was thus proven to contribute no additional discrimination ability to the detector. However, a different polarised material with higher nuclear spin to nuclear mass ratio will be able to experience stronger modulation effects. In the annual scale, the modulation effects of DM signal are also shown to be smaller than the absolute uncertainty. In conclusion, neither of these effects will be able to enhance discrimination in a polarized frozen Xenon detector.

Further studies can now be conducted using the particle generation algorithm and the generated directional data. By adjusting the differential rate equation to accommodate alternative target nuclei the success of different materials can be explored.

References

[1] M. W. Goodman and E. Witten, "Detectability of certain dark-matter candidates," *Phys. Rev. D* **31** (Jun, 1985) 3059–3063.

[2] A. K. Drukier, K. Freese, and D. N. Spergel, "Detecting cold dark-matter candidates," *Phys. Rev. D* **33** (Jun, 1986) 3495–3508.

[3] C. A. J. O'Hare, "Dark matter astrophysical uncertainties and the neutrino floor," *Phys. Rev.* **D94** no. 6, (2016) 063527, arXiv:1604.03858 [astro-ph.CO].

[4] P. Grothaus, M. Fairbairn, and J. Monroe, "Directional Dark Matter Detection Beyond the Neutrino Bound," *Phys. Rev.* **D90** no. 5, (2014) 055018, arXiv:1406.5047 [hep-ph].

[5] T. Franarin and M. Fairbairn, "Reducing the solar neutrino background in dark matter searches using polarized helium-3," *Phys. Rev.* **D94** no. 5, (2016) 053004, arXiv:1605.08727 [hep-ph].

[6] N. Bozorgnia, "Daily Modulation of the Dark Matter Signal in Crystalline Detectors," *ArXiv e-prints* (Sept., 2011) , arXiv:1109.0735 [astro-ph.IM].

[7] S. van den Bergh, "The Early history of dark matter," *Publ. Astron. Soc. Pac.* **111** (1999) 657, arXiv:astro-ph/9904251 [astro-ph].

[8] M. Milgrom, "A modification of the Newtonian dynamics as a possible alternative to the hidden mass hypothesis," **270** (July, 1983) 365–370.

[9] F. Zwicky, "Republication of: The redshift of extragalactic nebulae," *General Relativity and Gravitation* **41** no. 1, (2009) 207–224.

[10] S. Smith, "The Mass of the Virgo Cluster," **83** (Jan., 1936) 23.

[11] H. W. Babcock, "The rotation of the Andromeda Nebula," *Lick Observatory Bulletin* **19** (1939) 41–51.

[12] V. C. Rubin and W. K. Ford, Jr., "Rotation of the Andromeda Nebula from a Spectroscopic Survey of Emission Regions," **159** (Feb., 1970) 379.

[13] K. G. Begeman, A. H. Broeils, and R. H. Sanders, "Extended rotation curves of spiral galaxies: Dark haloes and modified dynamics," *Mon. Not. Roy. Astron. Soc.* **249** (1991) 523.

[14] S. Yoshiaki and V. Rubin, "Rotation curves of spiral galaxies," *Ann. Rev. Astron. Astrophys.* **39** (2001) 137–174, arXiv:astro-ph/0010594 [astro-ph].

[15] A. Jenkins *et al.*, "The mass function of dark matter haloes," *Monthly Notices of the Royal Astronomical Society* **321** no. 2, (2001) 372.

[16] J. F. Navarro, C. S. Frenk, and S. D. M. White, "The Structure of Cold Dark Matter Halos," astro-ph/9508025.

[17] D. Clowe *et al.*, "A direct empirical proof of the existence of dark matter," *The Astrophysical Journal Letters* **648** no. 2, (2006) L109. http://stacks.iop.org/1538-4357/648/i=2/a=L109.

[18] J. R. Primack, "Dark matter and structure formation," in *Midrasha Mathematicae in Jerusalem: Winter School in Dynamical Systems Jerusalem, Israel, January 12-17, 1997*.

[19] V. Springel *et al.*, "Simulating the joint evolution of quasars, galaxies and their large-scale distribution," *Nature* **435** (2005) 629–636, arXiv:astro-ph/0504097 [astro-ph].

[20] G. Hinshaw *et al.*, "Nine-year Wilkinson Microwave Anisotropy Probe (WMAP) Observations: Cosmological Parameter Results," **208** (Oct., 2013) 19, arXiv:1212.5226.

[21] **Planck** Collaboration, P. A. R. Ade *et al.*, "Planck 2015 results. XIII. Cosmological parameters," *Astron. Astrophys.* **594** (2016) A13, arXiv:1502.01589 [astro-ph.CO].

[22] B. D. Fields, K. Freese, and D. S. Graff, "Massive compact halo objects viewed from a cosmological perspective: Contribution to the baryonic mass density of the universe," *New Astron.* **3** (1998) 347–361, arXiv:astro-ph/9804232 [astro-ph].

[23] M. Taoso, G. Bertone, and A. Masiero, "Dark Matter Candidates: A Ten-Point Test," *JCAP* **0803** (2008) 022, arXiv:0711.4996 [astro-ph].

[24] G. Bertone, D. Hooper, and J. Silk, "Particle dark matter: Evidence, candidates and constraints," *Phys. Rept.* **405** (2005) 279–390, arXiv:hep-ph/0404175 [hep-ph].

[25] K. Jedamzik and M. Pospelov, "Big Bang Nucleosynthesis and Particle Dark Matter," *New J. Phys.* **11** (2009) 105028, arXiv:0906.2087 [hep-ph].

[26] E.-K. Park, "Contribution to dmsag report." http://science.energy.gov/hep/hepap/reports/, 2007. Accessed on: 2017-03-18.

[27] D. G. Cerdeno and A. M. Green, "Direct detection of WIMPs," arXiv:1002.1912 [astro-ph.CO].

[28] L. Bergstrom, P. Ullio, and J. H. Buckley, "Observability of gamma-rays from dark matter neutralino annihilations in the Milky Way halo," *Astropart. Phys.* **9** (1998) 137–162, arXiv:astro-ph/9712318 [astro-ph].

[29] J. I. Read, "The Local Dark Matter Density," *J. Phys.* **G41** (2014) 063101, arXiv:1404.1938 [astro-ph.GA].

[30] A. M. Green, "Dependence of direct detection signals on the wimp velocity distribution," *Journal of Cosmology and Astroparticle Physics* **2010** no. 10, 034.

[31] R. Schoenrich, J. Binney, and W. Dehnen, "Local kinematics and the local standard of rest," *Monthly Notices of the Royal Astronomical Society* **403** no. 4, (2010) 1829.

[32] A. M. Green, "Effect of realistic astrophysical inputs on the phase and shape of the weakly interacting massive particles annual modulation signal," *Phys. Rev. D* **68** (Jul, 2003) 023004.

[33] "Dark matter research at the university of shefield." https://www.hep.shef.ac.uk/research/dm/intro.php. Accessed on: 2017-03-18.

[34] G. Jungman, M. Kamionkowski, and K. Griest, "Supersymmetric dark matter," *Phys. Rept.* **267** (1996) 195–373, arXiv:hep-ph/9506380 [hep-ph].

[35] K. Griest, "Calculations of rates for direct detection of neutralino dark matter," *Phys. Rev. Lett.* **61** (Aug, 1988) 666–669.

[36] L. Vietze *et al.*, "Nuclear structure aspects of spin-independent WIMP scattering off xenon," *Phys. Rev.* **D91** no. 4, (2015) 043520, arXiv:1412.6091 [nucl-th].

[37] A. L. Fitzpatrick, W. Haxton, E. Katz, N. Lubbers, and Y. Xu, "The Effective Field Theory of Dark Matter Direct Detection," *JCAP* **1302** (2013) 004, arXiv:1203.3542 [hep-ph].

[38] V. Barger, W.-Y. Keung, and G. Shaughnessy, "Spin Dependence of Dark Matter Scattering," *Phys. Rev.* **D78** (2008) 056007, arXiv:0806.1962 [hep-ph].

[39] P. Klos, J. Menéndez, D. Gazit, and A. Schwenk, "Large-scale nuclear structure calculations for spin-dependent WIMP scattering with chiral effective field theory currents," *Phys. Rev.* **D88** no. 8, (2013) 083516, arXiv:1304.7684 [nucl-th]. [Erratum: Phys. Rev.D89,no.2,029901(2014)].

[40] U. T. Marrodan and L. Rauch, "Dark matter direct-detection experiments," *J. Phys.* **G43** no. 1, (2016) 013001, arXiv:1509.08767 [physics.ins-det].

[41] **LUX** Collaboration, D. S. Akerib *et al.*, "Results from a search for dark matter in the complete LUX exposure," *Phys. Rev. Lett.* **118** no. 2, (2017) 021303, arXiv:1608.07648 [astro-ph.CO].

[42] **XENON** Collaboration, E. Aprile *et al.*, "Physics reach of the XENON1T dark matter experiment," *JCAP* **1604** no. 04, (2016) 027, arXiv:1512.07501 [physics.ins-det].

[43] **PandaX-II** Collaboration, C. Fu *et al.*, "Spin-Dependent Weakly-Interacting-Massive-Particle–Nucleon Cross Section Limits from First Data of PandaX-II Experiment," *Phys. Rev. Lett.* **118** no. 7, (2017) 071301, arXiv:1611.06553 [hep-ex].

[44] J. Liu and X. Collaboration, "The xmass experiment," *AIP Conference Proceedings* **1604** no. 1, (2014) 397–401.

[45] **LZ** Collaboration, D. S. Akerib *et al.*, "LUX-ZEPLIN (LZ) Conceptual Design Report," arXiv:1509.02910 [physics.ins-det].

[46] **DARWIN Consortium** Collaboration, L. Baudis, "DARWIN: dark matter WIMP search with noble liquids," *J. Phys. Conf. Ser.* **375** (2012) 012028, arXiv:1201.2402 [astro-ph.IM].

[47] F. Mayet *et al.*, "A review of the discovery reach of directional Dark Matter detection," *Phys. Rept.* **627** (2016) 1–49, arXiv:1602.03781 [astro-ph.CO].

[48] E. Daw *et al.*, "The DRIFT Directional Dark Matter Experiments," *EAS Publ. Ser.* **53** (2012) 11–18, arXiv:1110.0222 [physics.ins-det].

[49] C.-T. Chiang, M. Kamionkowski, and G. Z. Krnjaic, "Dark Matter Detection with Polarized Detectors," *Phys. Dark Univ.* **1** (2012) 109–115, arXiv:1202.1807 [astro-ph.CO].

[50] I. G. Irastorza *et al.*, "Prospects for solar axions searches with crystals via Bragg scattering," *Nucl. Phys. Proc. Suppl.* **87** (2000) 102–104, arXiv:astro-ph/9912491 [astro-ph].

[51] J. Yoo *et al.*, "Scalability, Scintillation Readout and Charge Drift in a Kilogram Scale Solid Xenon Particle Detector," arXiv:1410.6496 [physics.ins-det].

[52] J. Yoo and W. F. Jaskierny, "Electron Drift in a Large Scale Solid Xenon," *JINST* **10** no. 08, (2015) P08011, arXiv:1508.05903 [physics.ins-det].

[53] J. Yoo *et al.*, "Scalability Study of Solid Xenon," *JINST* **10** no. 04, (2015) P04009, arXiv:1508.05897 [physics.ins-det].

[54] E. V. Krjukov, J. D. O'Neill, and J. R. Owers-Bradley, "Brute force polarization of 129xe," *Journal of Low Temperature Physics* **140** no. 5, (2005) 397–408.

[55] G. D. Cates, D. R. Benton, M. Gatzke, W. Happer, K. C. Hasson, and N. R. Newbury, "Laser production of large nuclear-spin polarization in frozen xenon," *Phys. Rev. Lett.* **65** (Nov, 1990) 2591–2594.

[56] "Review of mathematics, numerical factors, and corrections for dark matter experiments based on elastic nuclear recoil," *Astroparticle Physics* **6** no. 1, (1996) 87 – 112.

[57] **LUX** Collaboration, D. S. Akerib *et al.*, "Results on the Spin-Dependent Scattering of Weakly Interacting Massive Particles on Nucleons from the Run 3 Data of the LUX Experiment," *Phys. Rev. Lett.* **116** no. 16, (2016) 161302, arXiv:1602.03489 [hep-ex].

[58] P. Cushman *et al.*, "Working Group Report: WIMP Dark Matter Direct Detection," in *Proceedings, 2013 Community Summer Study on the Future of U.S. Particle Physics: Snowmass on the Mississippi (CSS2013): Minneapolis, MN, USA, July 29-August 6, 2013*.

[59] J. Barranco, O. G. Miranda, and T. I. Rashba, "Probing new physics with coherent neutrino scattering off nuclei," *JHEP* **12** (2005) 021, arXiv:hep-ph/0508299 [hep-ph].

[60] A. J. Anderson, J. M. Conrad, E. Figueroa-Feliciano, K. Scholberg, and J. Spitz, "Coherent Neutrino Scattering in Dark Matter Detectors," *Phys. Rev.* **D84** (2011) 013008, arXiv:1103.4894 [hep-ph].

[61] R. Brun and F. Rademakers, "Root - an object oriented data analysis framework," in *AIHENP'96 Workshop, Lausane*, vol. 389, pp. 81–86. 1996.

[62] M. A. Hapgood, "Space physics coordinate transformations - A user guide," **40** (May, 1992) 711–717.

[63] **SNO** Collaboration, B. Aharmim *et al.*, "Combined Analysis of all Three Phases of Solar Neutrino Data from the Sudbury Neutrino Observatory," *Phys. Rev.* **C88** (2013) 025501, arXiv:1109.0763 [nucl-ex].

[64] **Borexino Collaboration** Collaboration, G. Bellini *et al.*, "Final results of borexino phase-i on low-energy solar neutrino spectroscopy," *Phys. Rev. D* **89** (Jun, 2014) 112007.

[65] J. N. Bahcall, A. M. Serenelli, and S. Basu, "New solar opacities, abundances, helioseismology, and neutrino fluxes," *Astrophys. J.* **621** (2005) L85–L88, arXiv:astro-ph/0412440 [astro-ph].

[66] A. Drukier and L. Stodolsky, "Principles and applications of a neutral-current detector for neutrino physics and astronomy," *Phys. Rev. D* **30** (Dec, 1984) 2295–2309. http://link.aps.org/doi/10.1103/PhysRevD.30.2295.

[67] D. Z. Freedman, "Coherent effects of a weak neutral current," *Phys. Rev. D* **9** (Mar, 1974) 1389–1392.

[68] **SuperCDMS** Collaboration, R. Agnese *et al.*, "Projected Sensitivity of the SuperCDMS SNOLAB experiment," *Submitted to: Phys. Rev. D* (2016) , arXiv:1610.00006 [physics.ins-det].

[69] L. Baudis, A. Ferella, A. Kish, A. Manalaysay, T. Marrodan Undagoitia, and M. Schumann, "Neutrino physics with multi-ton scale liquid xenon detectors," *JCAP* **1401** (2014) 044, arXiv:1309.7024 [physics.ins-det].

[70] K. Lang, *Astrophysical Formulae: Volume I & Volume II: Radiation, Gas Processes and High Energy Astrophysics / Space, Time, Matter and Cosmology*. Astronomy and Astrophysics Library. Springer Berlin Heidelberg, 2006. https://books.google.ca/books?id=4BiCDQEACAAJ.

[71] "Solar position algorithm for solar radiation applications," *Solar Energy* **76** no. 5, (2004) 577 – 589.

Appendices

A Dark Matter Interaction Rate

In the first stages of this study the importance of a strong understanding in the arguments leading to a differential rate equation were identified. In this section, beginning from elastic collision kinematics, the fundamental components necessary to build a differential rate equation are derived. These are used in Section 2.5 of the main text.

A.1 Two Body Elastic Collision

An incoming DM particle colliding with a stationary target nucleus is assumed.

A.1.1 Velocity of CoM

The derivation of the location and velocity of the CoM of the two particle system is outlined below.

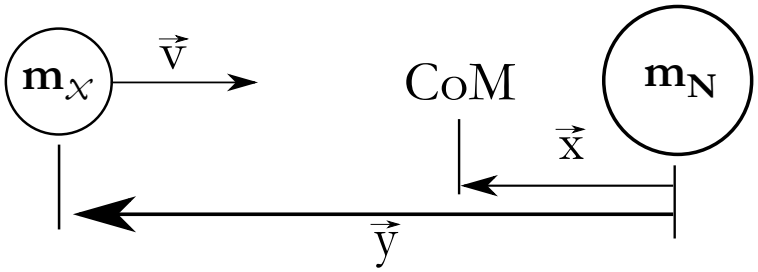

Figure A.1. Collision of a DM particle mass m_χ and stationary target nucleus m_N.

$$m_N\,\vec{x} = m_\chi\,(\vec{y}-\vec{x}) \;\;;\;\; \vec{x} \;= \frac{m_\chi}{m_N+m_\chi}\,\vec{y}$$
$$\vec{v}_{\text{CoM}} = \frac{d\vec{x}}{dt} = \frac{m_\chi}{m_N+m_\chi}\,\frac{d\vec{y}}{dt} = \frac{m_\chi\,\vec{v}}{m_N+m_\chi} \tag{A.1}$$

$$\mu_N = \frac{m_\chi m_N}{m_N+m_\chi} \;\;;\;\; \vec{v}_{\text{CoM}} = \frac{\mu_N \vec{v}}{m_N} \tag{A.2}$$

A.1.2 Final Kinetic Energy of Target

Since the target is stationary in the laboratory frame its velocity components in the CoM frame are as follows. $\vec{v}_N^{\,\mathrm{CoM}} = -\vec{v}_{\mathrm{CoM}}$.

$$\begin{aligned} \text{Horizontal final vel. of target in CoM frame: } u_N^{x\mathrm{CoM}} &= |\vec{v}_{\mathrm{CoM}}|\cos\theta \\ \text{Vertical final vel. of target in CoM frame: } u_N^{y\mathrm{CoM}} &= |\vec{v}_{\mathrm{CoM}}|\sin\theta \end{aligned} \tag{A.3}$$

Defining the velocity of the incoming DM particle to be in x-direction (horizontal), the components of the final velocity of the target in the laboratory frame can be calculated.

$$\begin{aligned} \text{Horizontal final vel. of target in laboratory frame: } u_N^{x\mathrm{Lab}} &= |\vec{v}_{\mathrm{CoM}}|\cos\theta - |\vec{v}_{\mathrm{CoM}}| \\ \text{Vertical final vel. of target in laboratory frame: } u_N^{y\mathrm{Lab}} &= |\vec{v}_{\mathrm{CoM}}|\sin\theta \end{aligned} \tag{A.4}$$

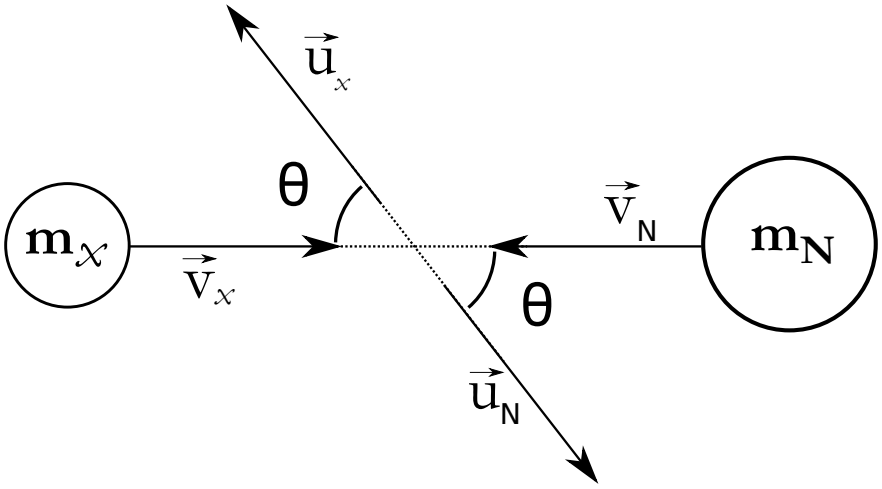

Figure A.2. Collision in the CoM frame by scattering angle θ.

The final kinetic energy of the target nucleus in the laboratory frame is then equal to the total energy transfered during the recoil E_{NR} assuming an elastic collision.

$$\begin{aligned} E_{NR} &= \frac{m_N}{2}\left(\left|u_N^{x\mathrm{Lab}}\right|^2 + \left|u_N^{y\mathrm{Lab}}\right|^2\right) \\ &= \frac{m_N|\vec{v}_{CoM}|^2}{2}\left((\cos\theta-1)^2+\sin^2\theta\right) \\ &= m_N|\vec{v}_{CoM}|^2(1-\cos\theta) \\ &= \frac{\mu_N^2|\vec{v}|^2}{m_N}(1-\cos\theta) \\ &= \frac{\mu_N^2 v^2}{m_N}(1-\cos\theta) \end{aligned} \tag{A.5}$$

A.2 Interaction Probabilities

A.2.1 Probability density for impact parameter b

It is assumed that a DM particle is destined to hit the target and that it is equally likely for it to hit any point within the target's physical cross-section. The probability is assumed to be proportional to the radial distance of the point of contact b, and then normalised to one.

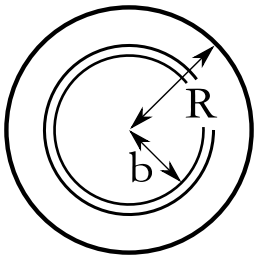

Figure A.3. The physical cross-section of the target nucleus of total radius R

$$\begin{gathered} p(b) = Ab \\ \int_{b=0}^{R} p(b)\, db = A\int_{b=0}^{R} b\; db = \frac{AR^2}{2} = 1 \\ A = \frac{2}{R^2} \quad ; \quad p(b) = \frac{2b}{R^2} \end{gathered} \tag{A.6}$$

A.2.2 Relationship between b and θ

Identifying the relationship between the scattering angle and the impact parameter from Figure A.4, the following can be written.

$$\begin{gathered} 2\phi = \pi + \theta \;\; ; \;\; \phi = +\frac{\theta}{2} = \beta + \frac{\pi}{2} \\ \beta = \frac{\theta}{2} \;\; ; \;\; \cos\frac{\theta}{2} = \frac{b}{R} \end{gathered} \tag{A.7}$$

Which can then be used in combination with the double angle trigonometric identity to derive the following.

$$\begin{aligned} 1-\cos\theta &= 1-\left(\cos^2\frac{\theta}{2} - \sin^2\frac{\theta}{2}\right) \\ &= 1-\left(2\cos^2\frac{\theta}{2} - 1\right) \\ &= 2\left(1-\cos^2\frac{\theta}{2}\right) \\ &= 2\left(1-\left(\frac{b}{R}\right)^2\right) \end{aligned} \tag{A.8}$$

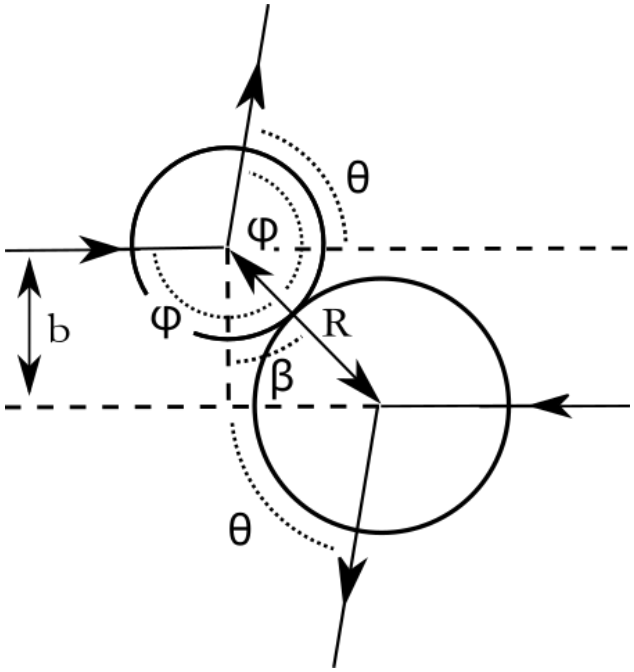

Figure A.4. Representation of the scattering event in the plane of collision.

A.2.3 Recoil Energy in terms of x=b/R

From Equations A.5, A.7 and A.8 it can be shown that,

$$E_{NR} = \frac{2\mu_N^2 v^2}{m_N}\left(1-\left(\frac{b}{r}\right)^2\right) \quad ; \quad x = \frac{b}{R}$$
$$E_{NR} = \frac{2\mu_N^2 v^2}{m_N}\left(1-x^2\right) \tag{A.9}$$

A.2.4 Probability Distribution of Recoil Energy

Remembering Equation A.6 and using change of variables,

$$p\left(\frac{b}{R}\right)\left|d\left(\frac{b}{R}\right)\right| = p(b)|db| \quad ; \quad p\left(\frac{b}{R}\right) = \frac{p(b)}{\left|\frac{d\left(\frac{b}{R}\right)}{db}\right|}$$
$$p\left(\frac{b}{R}\right) = R\,p(b) \quad ; \quad p(x) = 2x. \tag{A.10}$$

Remembering Equation A.9 and using change of variables once more,

$$
\begin{aligned}
p(E_{NR})|dE_{NR}| &= p(x)|dx| \\
p(E_{NR}) = \frac{p(x)}{\left|\frac{dE_{NR}(x)}{dx}\right|} \quad ; \quad \left|\frac{dE_{NR}(x)}{dx}\right| &= \frac{4\mu_N^2 v^2 x}{m_N} \\
p(E_{NR}) &= \frac{m_N}{2\mu_N^2 v^2}.
\end{aligned}
\tag{A.11}
$$

Since this probability was calculated assuming a collision has occurred, a final adjustment need to be made to introduce appropriate notation,

$$
p(E_{NR}|C) = \frac{m_N}{2\mu_N^2 v^2}. \tag{A.12}
$$

It is interesting to note that this probability does not depend on nuclear recoil energy.

A.3 Rate of collisions

In its simplest and most general form, the interaction rate can be constructed as the product of the following quantities,

$$
r = \Phi A \; p(E_{NR} \cap C). \tag{A.13}
$$

Φ = Flux; number of incident wimps per unit cross-sectional area

A = Cross-sectional area of detector

$p(E_{NR} \cap C) = p(E_{NR}|C)\, p(C)$

A.3.1 Interaction probability and cross-section

Each nucleus will have an interaction probability which is represented by a Quantum Mechanical cross-section. The cross-section of the detector is then assumed to be the sum of all the individual cross-sections from the nuclei. Overlap is not considered to cause any issues because of the relatively small nature of the individual cross-sections.

$$
A \; p(C) = \frac{N\sigma_0}{L_D^2} \tag{A.14}
$$

N = Number of Nuclei per kg of detector

L_D^2 = Area of incidence of DM particles to the detector in m^2

σ_0 = QM crossetion of a nucleous in m^2

The total number of particles per kg can be expressed as a function of Avogadro's number to be,

$$N = 10^3 N_A. \tag{A.15}$$

It is also customary to define the cross-section in terms of barns. 1 barn = $10^{-28} m^2$

$$\sigma_0 = 10^{-40} \sigma_0^{pb} \tag{A.16}$$

Combining Equations A.14, A.15 and A.16,

$$A\ p(C) = \frac{10^{-37} N_A \sigma_0^{pb}}{L_D^2}. \tag{A.17}$$

A.3.2 DM particles flux through the detector

The incident particle flux depends primarily on the local halo characteristics and can be defined as,

$$\Phi = \frac{10^6 L_D^2 \langle v \rangle \rho_o}{m_\chi}. \tag{A.18}$$

$L_D^2 =$ Area of incidence of DM to the detector in m^2
$\langle v \rangle =$ expectation velocity of DM in kms^{-1}
$\rho_o =$ local DM density in $GeVc^{-2}cm^{-3}$
$m_\chi =$ DM particle mass $GeVc^{-2}$

A.3.3 Constructing Rate of Collisions

By substituting Equations A.12, A.17 and A.19 in Equation A.13 a naive approximation for the total rate can be constructed.

$$\begin{aligned} r &\approx \frac{10^6 L_D^2 \langle v \rangle \rho_o}{m_\chi} \frac{10^{-37} N_A \sigma_0^{pb}}{L_D^2} \frac{m_N}{2\mu_N^2 \langle v \rangle^2} \\ r &\approx \frac{10^{-31} m_N N_A \sigma_0^{pb} \rho_o}{2 m_\chi \mu_N^2 \langle v \rangle} \end{aligned} \tag{A.19}$$

B Frame of Reference Manipulation

This section follows the derivation presented in Reference [6] of the components implemented in the FoR manipulation.

B.1 Parametrisation

B.1.1 Local Apparent Sidereal Time

The Local Apparent Sidereal Time (LAST) needs to be defined as it is heavily implemented in the code. Defined in units of hours as

$$t_{Lab} = t_{GAST} + \frac{l_{Lab}}{15}. \tag{B.1}$$

it depends on the Lab's geographical longitude l_{Lab} measured in degrees in a positive eastward (negative westward) direction, and the Greenwich Apparent Sidereal Time t_{GAST}. An approximation to t_{GAST} can be obtain using a formula for the Greenwich mean sidereal time (accurate to 1.2 seconds),

$$t_{GAST} = (101.0307 + 36000.770T_0 + 15.04107UT)/15. \tag{B.2}$$

where UT is the Universal time in hours and,

$$T_0 = \frac{[MJD] - 55197.5}{36525.0}. \tag{B.3}$$

In the above, $[MJD]$ is defined as the integer component of the Modified Julian Time and is obtained through a standard algorithm with a historical date input, year-month-day.

B.1.2 The Sun's Ecliptic Longitude

As also defined in Reference [70], the Sun's ecliptic longitude is a measure of the projection of the location of the Sun on the ecliptic plane of the equatorial frame. Measured anticlockwise from the vernal equinox, increasing with time due to the Earth's anticlockwise orbit around the Sun. In units of degrees and is calculated to be,

$$\lambda^o(t) = L + (1.915 - 0.0048T_0) * \sin(g) + 0.020\sin(2g) \tag{B.4}$$

where $L = 281.0298 + 36000.77T_0 + 0.04107UT$, represents the average longitude of the Sun, adjusted for annual aberration and $g = 357.9258 + 35999.05T_0 + 0.04107UT$ is the mean polar angle of orbit.

B.2 Transformation Matrices

In this section, frame of reference transformations used in Section 3.1.1 are defined.

B.2.1 Galactic to Equatorial Frame Transformation

This matrix allows for vectors defined in the galactic rest frame to be transformed to the Equatorial.

$$T_{\text{Gal} \to \text{Equ}} = \begin{bmatrix} -0.06699 & -0.8728 & -0.4835 \\ 0.4927 & -0.4503 & 0.7446 \\ -0.8676 & -0.1883 & 0.4602 \end{bmatrix} \tag{B.5}$$

B.2.2 Equatorial to Laboratory Frame Transformation

To transform vectors from the equatorial to the laboratory frame one needs to take into account not only the latitude of the observer's location in degrees l^o_{Lab} but also the time dependent t_{Lab}.

$$T_{\text{Equ}\rightarrow\text{Lab}} = \begin{bmatrix} -\sin(l^o_{Lab})\cos(15t_{Lab}) & -\sin(l^o_{Lab})\sin(15t_{Lab}) & \cos(l^o_{Lab}) \\ \sin(15t_{Lab}) & \cos(15t_{Lab}) & 0 \\ \cos(15t_{Lab})\cos(l^o_{Lab}) & \cos(l^o_{Lab})\sin(t_{Lab}) & \sin(l^o_{Lab}) \end{bmatrix} \tag{B.6}$$

B.3 Position of Sun in the Sky

Following the calculations outlined in Reference [71], the position of the Sun in the equatorial frame can be computed to be,

$$\begin{aligned} \vec{R}^{Eq}_{Sun} = (& r\cos(\lambda^o(t))\,\hat{x}_g \\ & + r\sin(\lambda^o(t))\cos(\chi_o)\hat{y}_g \\ & + r\sin(\lambda^o(t))\sin(\chi_o)\hat{z}_g\ ). \end{aligned} \tag{B.7}$$

The term with dependence on $\chi_o = 23^o.4393 - 3^o.563 * 10^{-7}[MJD]$ is the correction for the obliquity whereas the parametrisation for r is,

$$\begin{aligned} r &= \sqrt{(cos(E)-\epsilon)^2 + (1.0-\epsilon^2)\sin^2(E)} \\ E &= M + \epsilon\sin(M)(1+\epsilon\cos(M)) \\ M &= 356.047 + 0.9856002585[MJD]. \end{aligned} \tag{B.8}$$

C Velocity Distribution Spectra

Visualisation of the position of the Sun and incident DM wind density are shown as produced by the particle generation software outlined in Section 3.

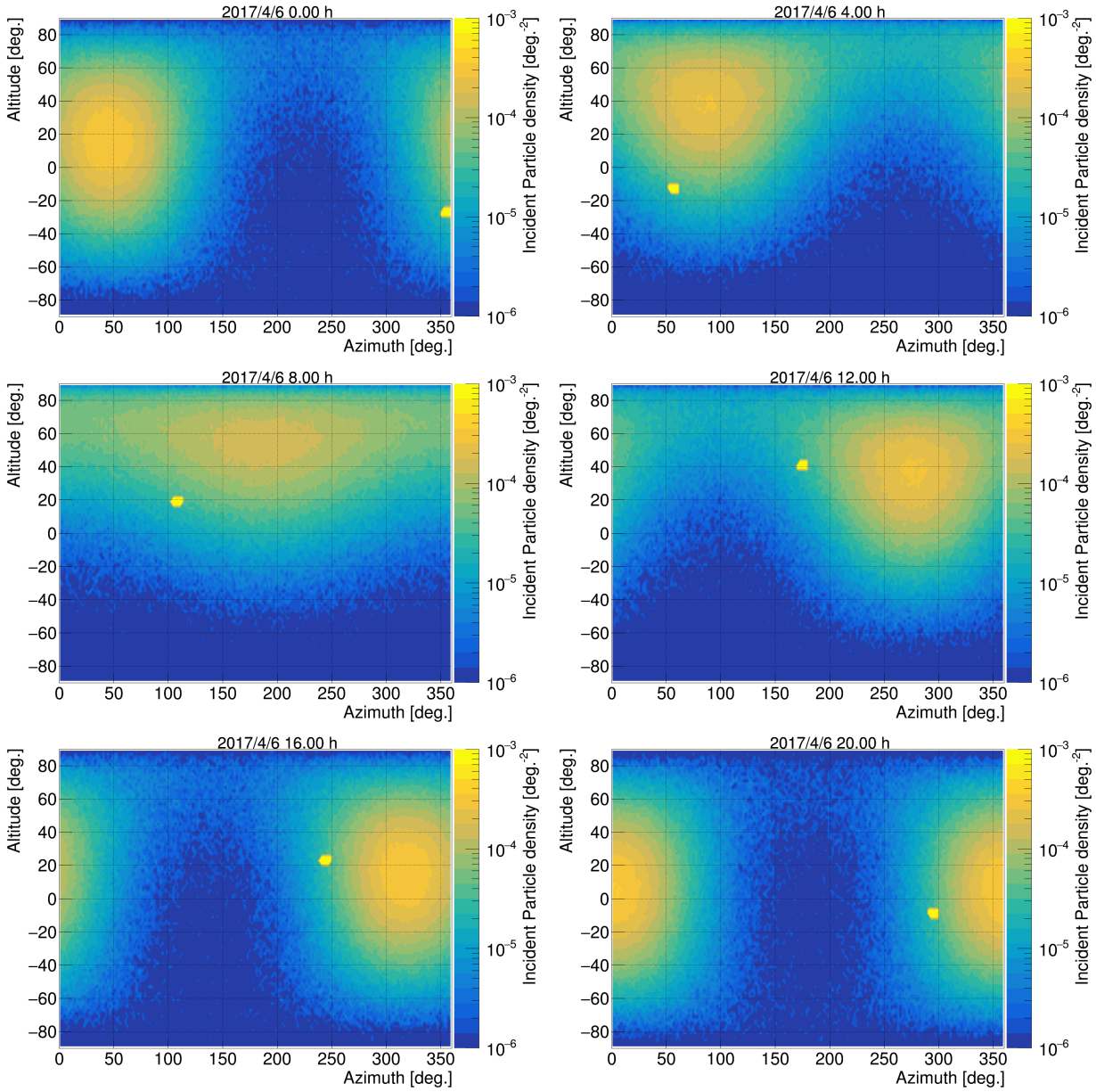

Figure C.1. The spacial distribution of insident DM particle density is plotted in the space of a spherical shell surrounding an observer with latitude $\lambda_{Lab} = 55^{o}.921731$ and longitude $l_{Lab} = -3^{o}.174090$. From left-to-right and top-to-bottom frames are shown representing the incident density of particles for 4 hour intervals for a total of a day. On the plot, $Altitude = 0$ overlaps with the horizon and the bright yellow circle represents the location of the Sun.

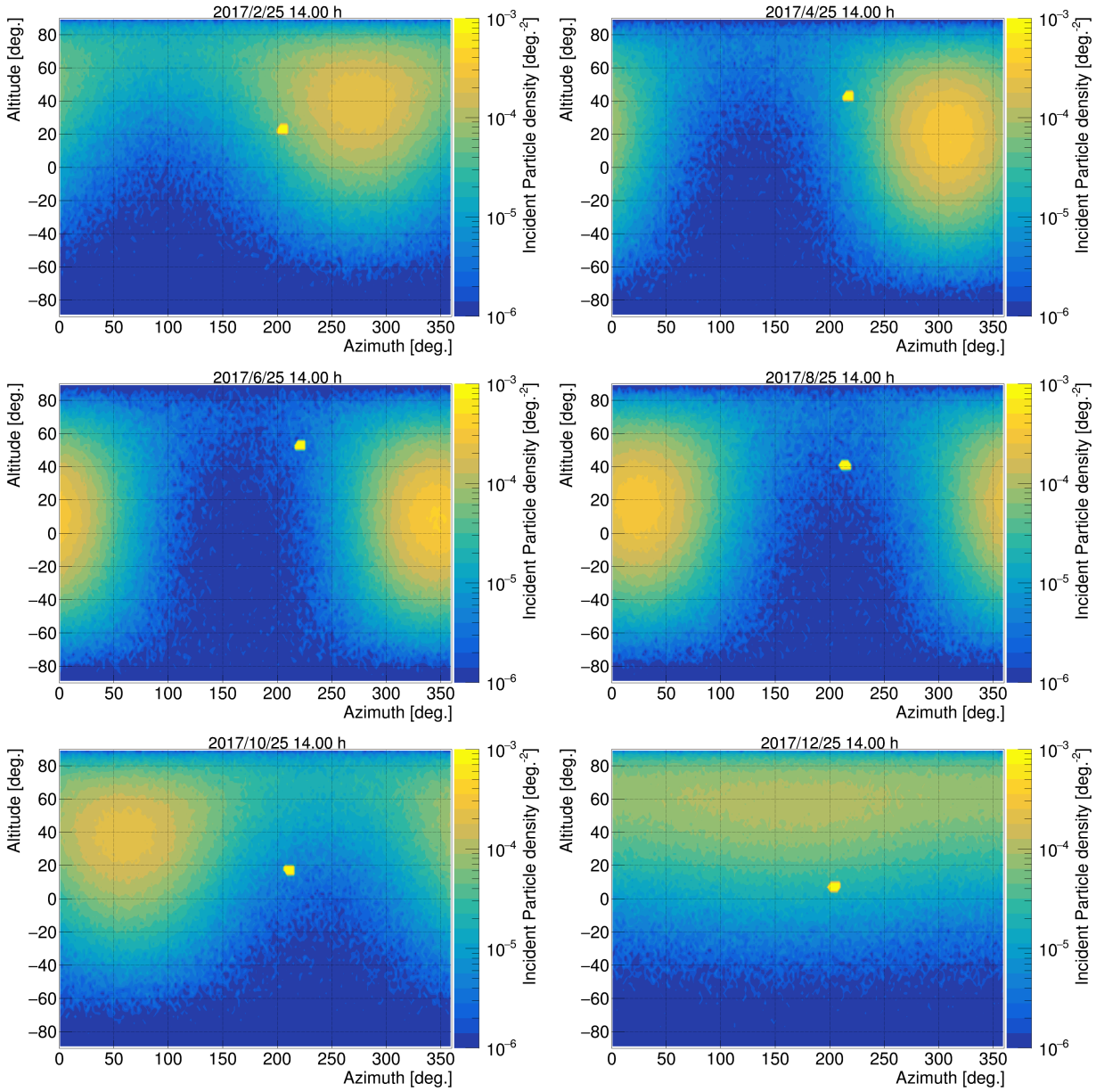

Figure C.2. The spacial distribution of incident DM particle density is plotted in the space of a spherical shell surrounding an observer with latitude $\lambda_{Lab} = 55^{o}.921731$ and longitude $l_{Lab} = -3^{o}.174090$. From left-to-right and top-to-bottom frames are shown representing the incident density of particles for 2 moth intervals for a total of a year. On the plot, $Altitude = 0$ overlaps with the horizon and the bright yellow circle represents the location of the Sun. The motion of the Sun in the period of a year, describes a Figure 8, also known as analemma.

D Neutrino Scattering Cross-Section

Here the full functional form of the neutrino coherent neutral-current scattering used in this study is presented as it was derived in Reference [5]. The angular-differential cross-section is,

$$\begin{aligned}\frac{d\sigma}{d\Omega} &= \frac{G_F^2 E_\nu^2}{16\pi^2}\{\sigma_{SI} + \sigma_{SD}\} \\ \sigma_{SI} &= c_V^2 + 3c_A^2 + \left(c_V^2 - c_A^2\right)\cos\psi \\ \sigma_{SD} &= -2c_A\left[(c_V - c_A)\,\hat{v}_\nu.\hat{s}_N + (c_V + c_A)\,\hat{v'}_\nu.\hat{s}_N\right],\end{aligned} \tag{D.1}$$

where G_F is the Fermi constant, ψ is the scattering angle, $\hat{v}_\nu$ and $\hat{v'}_\nu$ are the initial and final neutrino velocity vectors respectively, and $\hat{s}_N$ is the direction of nuclear polarisation. Equation D.1 also depends on the effective vectorial and axial couplings expressed as a function of the nucleon couplings to be $c_V = Zc_V^p + Nc_V^n$ and $c_A = c_A^{unpaired\ nucleon}$ respectively. The values of the individual nucleon couplings were set to be as shown in the table below.

	c_v	c_A
Proton	$1-4\sin^2\theta_W$	1.26
Neutron	-1	-1.26

The full differential cross-section was then set as,

$$\frac{d\sigma}{dE_{NR}} = \frac{2\pi}{m_N}\left(\frac{E_\nu + m_N}{E_\nu}\right)^2 \frac{d\sigma}{d\Omega} \tag{D.2}$$